



Self-consistent localized-orbital study of chemisorbed oxygen on Fe(001)
by Hong Huang

A thesis submitted in partial fulfillment of the requirements for the degree of Doctor of Philosophy in
Physics

Montana State University

© Copyright by Hong Huang (1985)

Abstract:

The electronic structure and magnetism of a $p(1 \times 1)$ chemisorbed oxygen layer on the Fe(001) surface was studied by the SCLO method. The interface geometry was suggested by a previous LEED analysis. We found a good agreement between the calculated DOS and the UPS data. We found the oxygen atoms have significant bonding to both the surface and subsurface Fe atoms, and atomic bonding pictures were derived. We did not find a magnetically dead layer of Fe surface, consistent with the spin-resolved photo emission experiments on Fe-based glass. The calculated work function change disagrees with the experiments, and this may be due to oxygen incorporation. The surface-state bands were predicted. Comparing these bands with ARPES may clarify the chemisorption/oxidation model.

SELF-CONSISTENT LOCALIZED-ORBITAL STUDY
OF CHEMISORBED OXYGEN ON FE(001)

by
Hong Huang

A thesis submitted in partial fulfillment
of the requirements for the degree

of
Doctor of Philosophy

in
Physics

MONTANA STATE UNIVERSITY
Bozeman, Montana

August 1985

Archives
D378
H86
Cop.1

ii

APPROVAL

of a thesis submitted by

Hong Huang

This thesis has been read by each member of the thesis committee and has been found to be satisfactory regarding content, English usage, format, citations, bibliographic style, and consistency, and is ready for submission to the College of Graduate Studies.

August 29, 1985
Date

John Hennerson
Chairperson, Graduate Committee

Approved for the Major Department

August 28, 1985
Date

Robert Swenson
Head, Major Department

Approved for the College of Graduate Studies

9-12-85
Date

W. Malone
Graduate Dean

STATEMENT OF PERMISSION TO USE

In presenting this thesis in partial fulfillment of the requirements for a doctoral degree at Montana State University, I agree that the Library shall make it available only for scholarly purposes, consistent with "fair use" as prescribed in the U.S. Copyright Law. Requests for extensive copying or reproduction of this thesis should be referred to University Microfilms International, 300 North Zeeb Road, Ann Arbor, Michigan 48106, to whom I have granted "the exclusive right to reproduce and distribute copies of the the dissertation in and from microfilm and the right to reproduce and distribute by abstract in any format."

Signature Hong Huang

Date 8/30/1985

ACKNOWLEDGEMENTS

The author gladly takes this opportunity to thank Professor John Hermanson, who suggested and supported the research reported here, for his unlimited advice and patient discussions during the past 3 years.

Helpful discussions with Jack Gay and John Smith of General Research Laboratories are greatly acknowledged.

TABLE OF CONTENTS

	page
APPROVAL.....	ii
STATEMENT OF PERMISSION TO USE.....	iii
ACKNOWLEDGMENT.....	iv
TABLE OF CONTENTS.....	v
LIST OF TABLES.....	vi
LIST OF FIGURES.....	vii
ABSTRACT.....	viii
CHAPTER 1. INTRODUCTION.....	1
CHAPTER 2. METHODOLOGY.....	11
Slab Model.....	11
Local Density Approximation.....	14
Matrix Form of the Schrodinger Equation.....	20
Gaussian Expansion of Atomic Wave Function and Potential.....	23
Starting-matrix Calculation.....	27
Symmetry.....	36
Self-consistent Iteration.....	51
Lowdin Representation.....	57
CHAPTER 3. RESULTS AND DISCUSSION.....	65
Two-level Bonding Model.....	65
Density of States.....	71
Atomic-orbital Occupancies.....	83
Magnetism.....	88
Charge and Spin Densities.....	89
Surface-state Bands.....	90
CHAPTER 4. SUMMARY AND FUTURE WORK.....	97
Summary.....	97
Suggestions for Future Study.....	98
REFERENCES CITED.....	100

LIST OF TABLES

	page
1. Atomic Wave Function and Point Group Representation.....	40
2. Representation matrices for C_{4v} Group.....	44
3. Representation matrix for Z-Reflection Group.....	45
4. Occupation Numbers for Fe, and O/Fe, Slabs.....	86
5. Magnetic Moments for Fe, and O/Fe, slabs.....	87

LIST OF FIGURES

	page
1. Slab model for $p(1 \times 1)$ O/Fe(001). Side View.....	12
2. Slab Model for $p(1 \times 1)$ O/Fe(001).Top view.....	13
3. Application of C_{4v} Symmetry.....	46
4. Application of Z-Reflection Symmetry.....	47
5. Two-level Bonding. Weak Coupling.....	69
6. Two-level Bonding. Strong Coupling.....	70
7. Layer-projected DOS's of O/Fe(001).....	76
8. Surface 3d-orbital DOS's of O/Fe(001).....	77
9. Subsurface 3d-orbital DOS's of O/Fe(001).....	78
10. Central-layer 3d-orbital DOS's of O/Fe(001).....	79
11. Planar Bonding I.....	80
12. Planar Bonding II.....	81
13. Vertical Bonding.....	82
14. Charge-density Contours.....	93
15. Spin-density Contours.....	94
16. Symmetric Surface Bands.....	95
17. Antisymmetric Surface Bands.....	96

ABSTRACT

The electronic structure and magnetism of a $p(1 \times 1)$ chemisorbed oxygen layer on the Fe(001) surface was studied by the SCLM method. The interface geometry was suggested by a previous LEED analysis. We found a good agreement between the calculated DOS and the UPS data. We found the oxygen atoms have significant bonding to both the surface and subsurface Fe atoms, and atomic bonding pictures were derived. We did not find a magnetically dead layer of Fe surface, consistent with the spin-resolved photoemission experiments on Fe-based glass. The calculated work function change disagrees with the experiments, and this may be due to oxygen incorporation. The surface-state bands were predicted. Comparing these bands with ARPES may clarify the chemisorption/oxidation model.

CHAPTER 1

INTRODUCTION

One of the major goals of surface science is to understand the microscopic mechanism of chemical corrosion, for which O/Fe is a very important example. The study of this system, however, was not possible until a few decades ago when ultra-high-vacuum techniques began to be applied so that the oxidation processes could be brought under control. Since then, extensive studies [1-15] have been performed on this system, both experimentally and theoretically. It is generally agreed that the dissociative chemisorption of oxygen on iron is the first step of oxidation of Fe, followed by incorporation of O into the selvedge to form a two-dimensional oxide. Finally this thin oxide layer begins to grow inward towards the bulk. However, there is no consensus regarding the adsorbed structure, the saturation coverage, the sticking probability, and the nature of the oxidation products, etc. Several experimental studies have been reported on the chemisorption and oxidation of the Fe(001) surface. Here we review them briefly.

Simmons and Dwyer [5] used low-energy-electron-diffraction (LEED) and Auger-electron spectroscopy (AES) to study the structural changes and kinetics of the oxidation of Fe(001) at room temperature. At first, the clean iron sample showed a sharp p(1x1) LEED pattern. When oxygen was deposited on the surface, half-order c(2x2) LEED spots gradually appeared, and their intensity and sharpness were maximized when AES indicated that half a monolayer of oxygen was formed on the surface. With further exposure (up to 10 L, 1 L=10⁻⁶ Torr-second), the half-order LEED spots gradually went away. The disappearance of the c(2x2) spots occurred simultaneously with the shift of the AES iron peaks. The LEED pattern became p(1x1) at 10 L, but the relative intensity of the integral-order spots was different from the corresponding diffraction features of the clean surface. This can be interpreted as (though the original interpretation of the authors was somewhat different) chemisorbed oxygen at alternate four-fold sites on the Fe(001) surface diffusing to sites beneath the Fe surface, followed by oxide nucleation. The shift of AES iron peaks indicated that the oxide is formed. This oxide, however, is amorphous rather than well ordered. The p(1x1) LEED pattern, therefore, is not due to this oxide but is due to the underlying iron substrate. The experiment also showed that further oxygen

exposure caused gradual weakening of all reflections, and no diffraction features were observed for exposures above 20 L. This is probably due to the fact that the amorphous oxide is thicker than the mean free path of the incident electrons, so no LEED pattern of the underlying Fe can be seen. After heating the sample mildly for a few minutes at this coverage, the $p(1 \times 1)$ LEED pattern showed up again. AES indicated that no change in oxygen concentration occurred during heating. The reappearance of LEED spots is interpreted as the result of a disorder-order transition of FeO. The epitaxial relationship between the FeO oxide layer and the Fe substrate is

$$(001)\text{FeO} \parallel (001)\text{Fe}.$$

AES also indicated that the concentration of oxygen at this stage was about 4 times higher than the value for the $c(2 \times 2)$ oxygen adlayer. This is exactly the amount of oxygen needed to form two layers of FeO with NaCl structure on the Fe substrate. The coincidence of the iron substrate and the oxide overlayer reflections suggests that the oxide has a lattice parameter 4.5% smaller than the value for FeO bulk. So it is expected that this epitaxial structure will change when the oxide layer becomes thicker. After 75 L exposure and mild heating of the sample, in addition to the spots of Fe(001), there

appeared hexagonal LEED spots which suggest an ordered FeO(111) layer epitaxially grown on the Fe(001) surface.

Brucker and Rhodin [8] studied the same system by using ultraviolet photoemission spectroscopy (UPS), LEED, and work-function-change measurements. For exposures less than 1.5 L, they reported little change (a small attenuation) of Fe d-band-peak emission compared to the corresponding data from a clean Fe sample. An additional peak centered about 5.5 eV below E_F appeared due to the 2p band of dissociatively chemisorbed oxygen. The LEED pattern at this stage showed a clear $0\ c(2 \times 2)$ structure on the Fe(001) surface. This was interpreted by the authors as confirming that a half monolayer of oxygen was formed on the Fe surface. The work function at this stage reached its maximum, about 0.2 eV above the clean surface value. For large exposures, the 5.5 eV peak broadened substantially, and the d-band emission was sharply attenuated. At 60 L the photoelectron energy distribution was very similar to that of FeO. Regarding the LEED patterns, further exposure caused the $c(2 \times 2)$ spots to fade out gradually at 4 L, and after that the $p(1 \times 1)$ spots disappeared at 7 L. The LEED pattern changes agreed well with those reported by Simmon and Dwyer, but not the exposures at which the LEED patterns changed. These changes suggest the beginning of the oxidation after 1.5 L.

exposure, and the formation of a few layers of amorphous oxide, as concluded by Simmon and Dwyer. The work function began to decrease after 1.5 L exposure, and reached a minimum value 0.05 eV higher than the work function of the clean Fe surface at 7 L exposure. This corresponds to the incorporation of oxygen beneath the iron surface, which leads to a reversal of the surface dipole, causing the work function to decrease. The authors concluded that below 1.5 L exposure, the system is in the dissociative chemisorption stage. Beyond that, a few layers of FeO are formed. Further exposure leads to the formation of a superstructure and the three-dimensional bulk oxide.

Legg, Jona, Jepson and Marcus [9] performed a LEED analysis in order to study the geometrical aspect of the chemisorption of oxygen on the Fe(001) surface. AES was also used to calibrate oxygen concentration on the surface and to monitor the possible existence of impurities. They reported that no fractional-order LEED spots were observed for oxygen chemisorbed on a clean Fe surface even when they varied oxygen-exposure procedures and thermal histories of the sample in order to produce the oxygen $c(2 \times 2)$ structure reported by other workers (Some faint half-order spots existed, but only when AES indicated the presence of large amounts of carbon on the surface). Exposure to oxygen caused no change in the geometry of the

LEED pattern but only changes in the intensities of the diffracted beams, consistent with the formation of the $0 \times 0 \times p(1 \times 1)$ structure on the Fe(001) substrate surface. The background remained low and contrast high up to 6-10 L, then the background increased and the LEED spots grew progressively broader with increasing exposure. After high exposures of 25 L or more, it was always possible to revert to the $0 \times 0 \times p(1 \times 1)$ structure by annealing it, but they never succeeded in reducing the oxygen concentration below one full monolayer by heating it. They found that 6 L oxygen exposure provided a complete and well ordered $p(1 \times 1)$ O/Fe(001) structure. By dynamical LEED calculation and intensity vs. voltage analysis, they determined that the O-Fe interlayer distance is 0.48 Å, with oxygen atoms occupying the 4-fold hollow sites in close proximity to substrate Fe atoms. The first Fe-Fe interlayer spacing is apparently expanded by 8% compared with bulk metal. This chemisorption model of O/Fe is shown in Fig.1 and Fig.2 except that the 7-layer slab geometry there should be replaced by semi-infinite geometry.

Recently, Sakisaka, Miyano and Onchi [10] used electron-energy-loss-spectroscopy (EELS) in conjunction with LEED, AES, secondary-electron emission spectroscopy (SES), and work-function-change measurements to study chemisorption and initial oxidation of Fe(001). Three

stages of oxidation were identified: (1) dissociative chemisorption below 3 L, (2) incorporation of O atoms into the selvedge between 3 and 20 L, and (3) oxidation above 20 L, leading to the formation of $\gamma\text{-Fe}_2\text{O}_3$. Of special interest is the change in surface electronic properties from that characteristic of the metal to that of the oxide observed by EELS. An energy-loss peak characteristic of the chemisorbed oxygen was observed at 6 eV below 3 L, being ascribed to the transition between the bonding and antibonding states. The clean surface energy-loss peaks at about 5 and 8 eV were weakened substantially at this stage, but the 2 eV energy-loss peak remained unchanged until the exposure was in the range at 3-20 L. The authors interpreted the former peaks as involving $\text{Fe } 3d_{xy, xz, yz}$ and the latter as involving $\text{Fe } 3d_{z^2, x^2-y^2}$. Thus the $\text{Fe } 3d_{xy, xz, yz}$ orbitals play a major role in the chemisorption bond, and for the incorporation process the $\text{Fe } 3d_{z^2, x^2-y^2}$ orbitals are involved. The EELS spectrum in the oxide phase was characterized by peaks due to the $\text{O}^{2-} 2p \rightarrow \text{Fe}^{3+} 3d$ charge-transfer transition. The $\gamma\text{-Fe}_2\text{O}_3 \rightarrow \text{FeO}$ phase transition at 570 C was also confirmed by monitoring an energy-loss peak due to a $d \rightarrow d$ transition. The work-function-change measurement showed that the work function increased steeply up to 3 L, reaching a maximum of $\Delta\Phi = +0.25$ eV at 3 L, then decreased

to a minimum of $\Delta\Phi = +0.02$ eV at 20 L, and finally increased again to a limiting value $\Delta\Phi = 0.4$ eV at 350 L. The initial increase of the work function is due to charge transfer to the chemisorbed oxygen, creating a surface dipole layer, thus increasing the energy barrier for electrons coming out of the surface. The subsequent decrease of the work function is due to the oxygen incorporation, leading to an oxide layer. The final increase of the work function is related to the in-depth oxidation. The work-function-change measurement thus agreed with the three-stage oxidation process confirmed by EELS analysis. The LEED pattern seen at the chemisorption stage is $p(1 \times 1)$, agreeing with the observation of Legg *et al* [9]. However, the coverage calibration, with 3 L exposure corresponding to a coverage of 0.35 and 20 L corresponding to a coverage of 1, does not agree with the calibration of any other group.

After reviewing the results of experimental investigations, it is realized that the geometrical aspect of oxidation is still controversial. For example, it is agreed that at some stage of oxidation there is a $p(1 \times 1)$ structure of the O/Fe(001) system. The question is: does this $p(1 \times 1)$ structure correspond to the chemisorption of oxygen on the Fe(001) surface, or to the incorporation of oxygen beneath the Fe(001) surface, forming amorphous or

ordered FeO? Although we know that the oxygen eventually goes inside the Fe surface, the exact nature, extent and geometry of the oxygen incorporation remains unknown. The task of theoretical investigation, therefore, is to pick some experimental models, to study and possibly to predict the properties of the system, to compare with further experiments, and then to justify or refine the model. We chose the model proposed by Legget et al for oxygen chemisorption on the Fe(001) surface.

A few electronic structure calculations have been performed using cluster models of the O/Fe(001) chemisorption system. In spin-polarized computations for the cluster O-Fe₅, Anderson [13] obtained oxygen 2p levels 6 eV below the highest occupied level, and an equilibrium Fe-O interlayer spacing of 0.48 Å, when the oxygen was placed in the four-fold hollow site. Ribarsky, in an unrestricted Hartree-Fock cluster calculation [14], predicted a vertical spacing of 0.38 Å. In recent X-ray cluster calculations [15], Adachi et al used a 9-atom substrate to study the level structure of O/Fe(001) versus the Fe-O bond site and bond length. For an interlayer spacing near 0.5 Å, three O 2p levels were obtained in the energy range 5 to 7 eV below E_F. The d-band density of states (DOS) was reduced near E_F due to the Fe-O bonding.

None of the calculations reviewed above included the effects of adsorbate-adsorbate interactions in the extended O/Fe(001) system. This interaction broadens the O 2p levels, leading to two-dimensional energy bands. These bands hybridize at general points in the irreducible wedge of the surface Brillouin zone (IBZ) but have definite reflection parity along the Σ and Δ symmetry lines. They should be detectable using angle-resolved photoemission spectroscopy (ARPES) [16]. The use of polarized light in conjunction with the selection rules [17] should aid in their identification.

Here we report calculations of the electronic structure of a p(1x1) O/Fe(001) slab using the self-consistent localized-orbital (SCLO) method developed by Smith, Gay and Arlinghaus [18-20]. In addition to the calculation of O/Fe(001) [21], we also did a number of slab calculations: Ni/Cu(001) [22], Cu/Ni(001) [23], H/Ni(001) [24], Pd/Fe(001) [25], and Fe/Cu(001) [26]. Because this method incorporates an atomic orbital basis, a simple picture of the surface bond can be developed from the numerical results. By treating electron-spin polarization explicitly, we were able to study the magnetic behavior of this system as well as the influence of the magnetism on the bonding and energy band structure. The SCLO method is discussed in detail in the next chapter.

CHAPTER 2

METHODOLOGY

Slab Model

The semi-infinite surface can be simulated theoretically by an atomic slab with infinite extension in the XY (surface) plane and a finite number of layers in the Z direction (normal to surface). See Fig.1 and Fig.2. In our study, we calculated electronic properties of the slab by applying the Schrodinger equation to it without any adjustable parameters. The only physical inputs are the atomic positions m and nuclear charges Z . Atomic positions are assumed to have translation symmetry in the XY plane and reflection symmetry in the Z direction. The slab may be considered thick enough to represent the real surface if the calculated electronic properties at the center layer are bulk like [27,28].

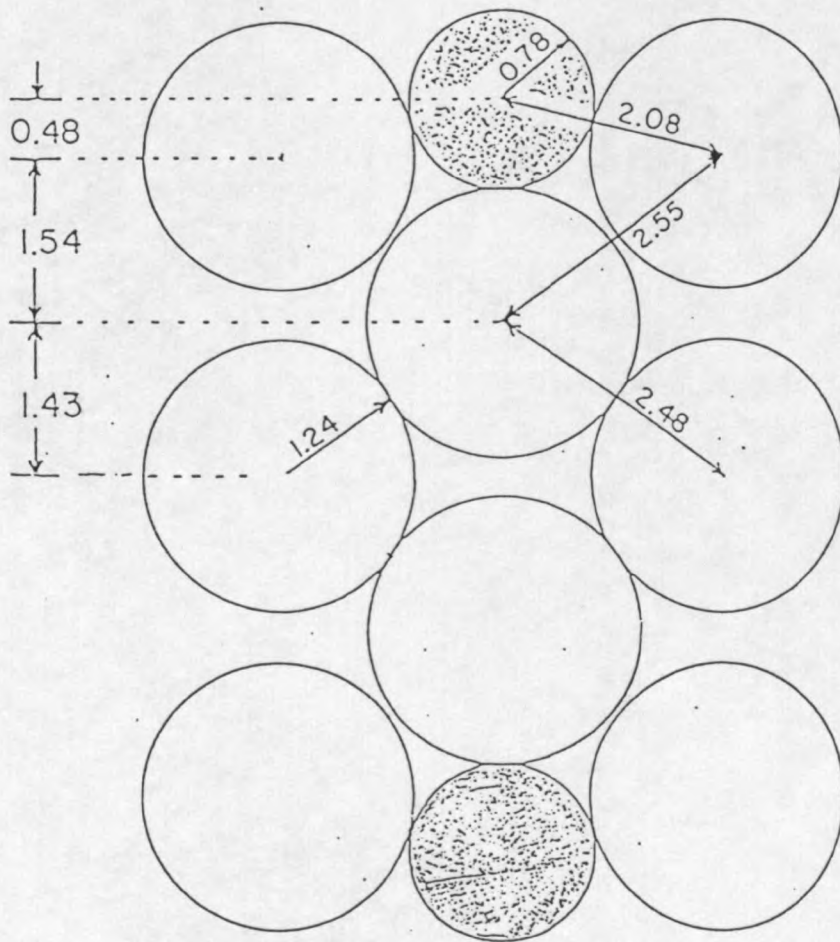


Fig.1 Slab model for p(1x1) O/Fe(001). Side View. Cross section along (110) plane. Distances in angstroms.

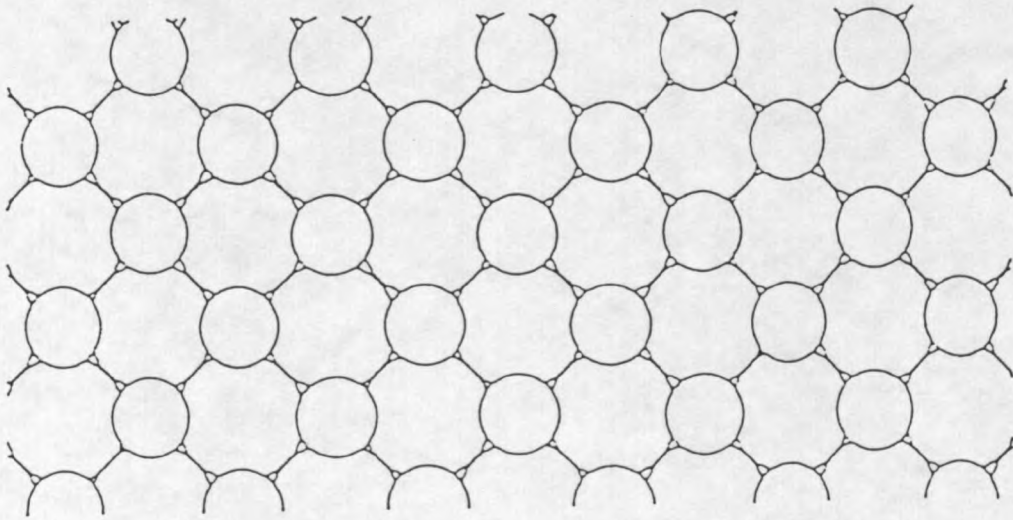


Fig.2 Slab model for p(1x1) O/Fe(001). Top View.

Local Density Approximation

The electronic wave function of the system obeys the Schrodinger equation

$$H \Psi(r_1, s_1, \dots, r_n, s_n) = E \Psi(r_1, s_1, \dots, r_n, s_n), \quad (1)$$

where

$$H = \sum_{i=1}^N \left(-\frac{1}{2} \nabla_i^2 - \sum_m \frac{Z_m}{|r_i - m|} \right) + \frac{1}{2} \sum_{i=1}^N \sum_{j=1}^N \frac{1}{r_{ij}}, \quad (2)$$

m is the atomic position and N is the number of electrons in the system. Atomic units (a.u.) are used. This is valid in the non-relativistic approximation, namely, for all elements with atomic number $Z < 50$ [27], thus including 3d and 4d transition metals, which we are most interested in.

In the single-electron approximation, due to Pauli's exclusion principle, the wave function can be written as a Slater determinant

$$\Psi(r_1, s_1, \dots, r_n, s_n) = \frac{1}{(n!)}^{1/2} \times \begin{vmatrix} \phi_1(1) & \dots & \phi_n(1) \\ \vdots & & \vdots \\ \phi_1(n) & \dots & \phi_n(n) \end{vmatrix}, \quad (3)$$

where

$$\phi_i(j) = \psi_i(r_j) \chi_i(s_j), \quad (4)$$

that is, the single-electron wave function is the product of an orbital function and a spin function.

To minimize the total energy of the system $\langle \Psi | H | \Psi \rangle$, the single-electron wave function must obey the Hartree-Fock equation [29,30,31]:

$$\begin{aligned} & [-1/2\nabla^2 - \sum_m Z_m / |r_i - m| + \sum_j \int \psi_j^*(r') \psi_j(r') d^3r' / |r - r'|] \psi_i(r) \\ & - \sum_j [\delta s_i s_j \int \psi_j^*(r') \psi_i(r') d^3r' / |r - r'|] \psi_j(r) = E \psi_i(r). \end{aligned} \quad (5)$$

The first term in this equation is the kinetic energy, the second one is the potential energy due to the nucleus, the third one is the Coulomb interaction potential between electrons, and the fourth one is exchange potential between parallel-spin electrons, due to Pauli's exclusion principle.

In the Local Density Approximation (LDA) [32-35], the exchange potential can be written as a function of the local electron density for each spin:

$$V_{x\uparrow\text{or}\downarrow} = -[(3/\pi)\rho_{\uparrow\text{or}\downarrow}(r)]^{1/3} \quad (6)$$

To derive the above expressions [36], first let us consider the extreme case of a homogeneous electron gas under the influence of a constant potential field. We can use plane waves to represent wave functions:

$$\psi_i(r) = \exp(ik_i \cdot r) \quad (7)$$

Then the exchange term in the Hartree-Fock equation becomes

$$\begin{aligned}
 & \sum_j \left[\int \exp(-i(\mathbf{k}_j - \mathbf{k}_i) \cdot \mathbf{r}') / |\mathbf{r} - \mathbf{r}'| d^3 r' \right] \exp(i\mathbf{k}_j \cdot \mathbf{r}) \\
 &= \left[\sum_j \int \exp(i(\mathbf{k}_j - \mathbf{k}_i) \cdot \mathbf{r}) / r d^3 r \right] \exp(i\mathbf{k}_i \cdot \mathbf{r}) \\
 &= 4\pi \left[\sum_{\mathbf{k}_j < \mathbf{k}_F} 1 / (\mathbf{k}_j - \mathbf{k}_i)^2 \right] \psi_i(\mathbf{r}) \\
 &\rightarrow 1 / (2\pi^2) \left[\int_{\mathbf{k}_j < \mathbf{k}_F} 1 / (\mathbf{k}_j - \mathbf{k}_i)^2 d^3 \mathbf{k}_j \right] \psi_i(\mathbf{r}) \\
 &= (\mathbf{k}_F / \pi) F(\mathbf{k}_i / \mathbf{k}_F) \psi_i(\mathbf{r}) \tag{8}
 \end{aligned}$$

where

$$F(x) = 1 + [(1-x^2)/2x] \ln |(1+x)/(1-x)|. \tag{9}$$

The exchange energy term is k_i -dependent. There are several ways to average this k_i -dependence, for example, inside the Fermi sphere $k_i < k_F$, which is the Slater approximation and which gives $\langle F \rangle = 1.5$ [37], or at the Fermi sphere $k_i = k_F$, which is the Kohn-Sham approximation and which gives $\langle F \rangle = 1$ [33]. We use the latter since it can be derived, alternatively, based on the variational principle thus in a more rigorous way [33].

The value of the Fermi wavevector is related to the charge density by

$$k_F = (3\pi^2 \rho)^{1/3} \tag{10}$$

for each spin since the summation in the exchange term of Eq.(5) is over a particular spin only. So the exchange energy for the homogeneous electron gas is given by the Eq.(6).

Now we consider the electrons moving in a slowly varying potential field. The fundamental assumption is that the above expression for exchange energy of a homogeneous system is valid locally even in the case of a slowly varying inhomogeneous system. This is the essential idea behind the Thomas-Fermi method for atoms [38,39]. It is expected that the LDA will be a good approximation for solids in the interstitial region, where the potential and the electron density do change slowly and where most of the charge rearrangement occurs when the solid is formed from isolated atoms.

The LDA is not only an approximation for the Hartree-Fock exchange potential, it also incorporates many-body correlation effects. The motion of electrons is highly correlated. Following each electron as it moves through the system is a depression in the distribution of other electrons. The depression is called the exchange-correlation hole. In the Hartree-Fock equation, the instantaneous interaction between any pair of electrons $1/r_{ij}$ is treated as the interaction between one electron and the distribution of another electron. In particular,

the two antiparallel-spin electrons are allowed to be at the exactly same space point (Slater determinant for two antiparallel-spin electrons does not vanish when $r_1=r_2$) which will never happen in the real physical system. Thus Coulomb interaction between electrons is overestimated in this way, especially in the high density region, although for parallel-spin electrons the exchange energy partly makes up this deficiency. Further improvement is needed for both parallel and antiparallel electrons by adding a term called the correlation energy to the Hamiltonian.

The correlation term in LDA is also a function of the local electron density of both spins, ρ_\uparrow and ρ_\downarrow , or equivalently, it is a function of r_s and p , where

$$r_s = [3 / (4\pi \times (\rho_\uparrow + \rho_\downarrow))]^{1/3}, \quad (11)$$

which is the average distance between electrons, and

$$p = (\rho_\uparrow - \rho_\downarrow) / (\rho_\uparrow + \rho_\downarrow), \quad (12)$$

which is the polarization parameter.

Our correlation potential was adapted from studies of the spin-polarized homogeneous electron liquid by Vosko, Wilk and Nusair [40]. They used a Pade technique to interpolate accurate results for the random-phase-approximation (RPA) [40-45] correlation energy, valid for small r_s , to low density, where Monte Carlo results

[46,47] are available. To determine a convenient form of the correlation energy, the paramagnetic correlation energy per electron [40] was first fitted as [48-50]

$$e(r_s, 0) = -AF(r_s/R), \quad (13)$$

where

$$F(x) = (1+x^3) \ln(1+1/x) + 2/x - x^2 - 1/3, \quad (14)$$

A is 48.6 mRy, and R is 15. We also fit the spin stiffness α to Eq.(13) with $A'=31.1$ mRy and $R'=16.4$. The spin-dependent correlation energy can be written as [40]

$$e(r_s, p) = e(r_s, 0) + \alpha p^2 / 2. \quad (15)$$

Then

$$\begin{aligned} & V_{\text{cfor}\downarrow} \\ &= \frac{\partial(\rho e_c)}{\partial \rho_{\uparrow} \text{or} \downarrow} \\ &= -A \ln(1+R/r_s) \pm \alpha p + \beta p^2, \end{aligned} \quad (16)$$

where

$$\beta = 1/2 A' \ln(1+R'/r_s) - \alpha. \quad (17)$$

To sum up, in LDA, the single-electron wave function obeys

$$[-1/2\nabla^2 - \sum_m Z_m / |\mathbf{r}-\mathbf{m}| + \int \rho(\mathbf{r}') d^3\mathbf{r}' / |\mathbf{r}-\mathbf{r}'| + V_{xc}(\rho(\mathbf{r})^{1/3})] \psi(\mathbf{r}) = E \psi(\mathbf{r}). \quad (18)$$

Symbolically,

$$H(\rho(\mathbf{r}))\psi = E\psi. \quad (19)$$

In order to know the wave function, we have to know $\rho(\mathbf{r})$ first. But $\rho(\mathbf{r})$ is given by

$$\rho(\mathbf{r}) = \sum_{\text{occupied}} \psi_i(\mathbf{r})^2. \quad (20)$$

So in order to know $\rho(\mathbf{r})$, we have to know $\psi_i(\mathbf{r})$ first. This indicates we have to solve Eq.(18) self-consistently.

Matrix Form of the Schrodinger Equation

The Schrodinger equation

$$H(\mathbf{r})\psi_j(\mathbf{r}) = E\psi_j(\mathbf{r}) \quad (21)$$

can be written in matrix form with an appropriate choice of basis. The basis functions we choose here are the Bloch lattice sums of atomic wave functions:

$$\phi_i(\mathbf{r}, \mathbf{k}) = \sum_m \exp(-i\mathbf{k}\cdot\mathbf{m}) a_i(\mathbf{r}-\mathbf{m}), \quad (22)$$

where \mathbf{k} is in the irreducible Surface Brillouin Zone, \mathbf{m} is a lattice site within one layer of the slab, and $a_i(\mathbf{r}-\mathbf{m})$ is the i th atomic wave function located at lattice site \mathbf{m} . The subscript i indicates both the atomic orbital and the

layer at which the atom is located. Since d-electrons of transition metals are tightly bound by the nucleus nearby, they behave somewhat like the corresponding atomic d-electrons. Therefore, the introduction of the lattice can be considered as a perturbation. Thus the atomic wave functions are good candidates for the basis set in this case. There are 19 atomic functions for each Fe atom in the cell: 1s, 2s, 2p, 3s, 3p, 3d, 4s, 4p, 5s, and 9 atomic functions for each O atom in the cell: 1s, 2s, 2p, 3s, 3p. Among them the Fe 4p, 5s and the O 3s, 3p orbitals are not occupied in isolated atoms. We add them to increase variational freedom [51] in describing charge rearrangement in the interstitial and surface regions of the solids. The extended virtual orbitals of the surface atom are especially important, for without them we could not describe the charge expansion into vacuum properly, and thus could not get the correct work function. Trial calculation shows that whether or not we include the Fe 4d orbitals is not crucial in the calculation.

The eigenfunction of the Schrodinger equation is expanded into atomic Bloch functions with a given k since k is a good quantum number:

$$\psi_j(r, k) = \sum_i c_{ij} \tilde{\phi}_i(r, k) \quad (23)$$

We plug (22) and (23) into (21), multiply $a_1(r)$ from the left, and perform the integration, obtaining

$$\sum_i [H_{1i}(k) - E_j O_{1i}(k)] c_{ij} = 0, \quad i=1, N \quad (24)$$

where

$$H_{1i}(k) = \sum_m \exp(-ik \cdot M) \langle a_1(r) | H(r) | a_i(r-M) \rangle, \quad (25)$$

$$O_{1i}(k) = \sum_m \exp(-ik \cdot M) \langle a_1(r) | a_i(r-M) \rangle. \quad (26)$$

Symbolically, the equation in matrix form is

$$HC = EOC. \quad (27)$$

This is a generalized diagonalization problem.

After we diagonalize (24) for every k , we get all $\psi_j(k)$ and $E_j(k)$. We then count energy levels $E_j(k)$ from low to high up to the total number of the valence electrons (the meaning of valence electron, as opposed to core electron, will be explained later) of the slab cell times the number of k points. Summing over all occupied states, we get the charge density, and thus the new potential. We keep running until the potential is self-consistent.

Gaussian Expansion of Atomic Wave Function and Potential

In the central-field approximation, the atomic wave function can be written as [29]

$$a(r) = R_{n,1}(r) Y_{1,m}(\theta, \phi), \quad (28)$$

where

$$R_{n,1}(r) = \sum_j D_{n,j} g_1(\alpha_j, r), \quad (29)$$

$$g_1(\alpha_j, r) = \frac{2^{1+7/4} \alpha_j^{1/2+3/4}}{\pi^{1/4} [1 \times 3 \times \dots \times (2l+1)]^{1/2}} r^1 \exp(-\alpha_j r^2), \quad (30)$$

and $g_1(\alpha_j, r)$ is a normalized radial Gaussian primitive [52]. What we want is a set of α_j and D_j ($j=1, N$) which best represents an atomic wave function with a given, finite N .

The procedure to get these α 's and D 's is as follows:

- 1) Solve the LDA Equation for an atom with a spherically symmetric potential $V(r)$,

$$V(r) = -Z/r + (4\pi/r) \int \rho(r') r'^2 dr' + V_{xc}(r), \quad (31)$$

obtaining the self-consistent $V(r)$ numerically [53].

- 2) Choose α 's for the Gaussian basis set as

$$\alpha_j = \alpha_1 \beta^{j-1} \quad j=1, N \quad (32)$$

These are even-tempered Gaussians [52] which almost cover the whole spectrum of relevant Gaussians.

- 3) Resolve the atomic LDA equation with matrix form [54] using the given Gaussian basis set:

$$\sum_j (H_{ij} - ES_{ij})D_j = 0, \quad i=1, N \quad (33)$$

obtaining $E_1 < E_2 < \dots < E_n$ and the corresponding D 's.

- 4) Vary α_1 and β , repeating 2) 3) above to minimize E_1 , to get the best α 's and D 's for Ψ_1 (1s).
- 5) Add two more Gaussians to the above basis, solve the $N+2$ dimensional equation of the atom, vary α_{n+1} and α_{n+2} to minimize E_2 , and use the Schmidt procedure to make this best 2s function orthogonal to the 1s function.
- 6) Repeat the procedure for all occupied atomic wave functions for a given angular momentum.
- 7) Repeat the procedure for all occupied atomic wave functions with different angular momenta.
- 8) Add virtual orbitals for s and p functions (a single diffuse Gaussian for each orbital) to provide maximum variational freedom in describing charge rearrangement when the atomic slab is constructed.

This describes how we obtain the atomic wave functions. Under the assumption of atomic configurations ($3d^7 4s^1$ for Fe and $2s^2 2p^4$ for O), we can determine the atomic charge

distribution, and therefore the atomic potential. The atomic potential can be separated into two parts [55]: the first one contains a singularity at the origin, and the second is finite everywhere, so it can be expanded into Gaussians:

$$V(r) = V_1(r) + V_2(r), \quad (34)$$

$$V_1(r) = -(Z/r) \exp(-r^2), \quad (35)$$

$$V_2(r) = (Z/r)(1 - \exp(-r^2)) + V_{\text{Coulomb}} + V_{\text{xc}}. \quad (36)$$

Now we are ready to expand V_2 into Gaussians. But before doing that, we first rename $V_2(r)$ as $V(r)$, and name its expansion as $V'(r)$:

$$V'(r) = \sum_j D_j g(\alpha_j, r), \quad (37)$$

where the α 's obey Eq. (32), that is, they are even-tempered Gaussians.

A least-squares-fitting procedure is used to optimize the expansion. That is, we try to find $V'(r)$ such that

$$\int [V(r) - V'(r)]^2 \omega(r) r^2 dr = \text{Min}, \quad (38)$$

where $\omega(r)$ is a weighting factor, and we set $\omega(r) = r$.

$V(r)$ and $V'(r)$ have to obey

$$\int V(r)^2 \omega(r) r^2 dr = \int V'(r)^2 \omega(r) r^2 dr = \text{Const}. \quad (39)$$

(38) with (39) is equivalent to

$$\int V(r)V'(r)\omega(r)r^2 dr = \text{Max.} \quad (40)$$

When (37) is used to expand $V'(r)$ in (40), we have

$$I(\alpha, D) = \sum_j D_j \int V(r)g(\alpha_j(r))\omega(r)r^2 dr = \sum_j D_j P_j = \text{Max.}, \quad (41)$$

where

$$P_j = \int V(r)g(\alpha_j, r)\omega(r)r^2 dr. \quad (42)$$

Squaring (40), we have

$$I^2(\alpha, D) = \sum_i \sum_j D_i D_j P_i P_j = \text{Max.} \quad (43)$$

(37) is also used to expand (39), and we have

$$\begin{aligned} & \sum_i \sum_j D_i D_j \int g(\alpha_i, r)g(\alpha_j, r)\omega(r)r^2 dr \\ &= \sum_i \sum_j D_i D_j S_{ij} = \text{Const.}, \end{aligned} \quad (44)$$

where

$$S_{ij} = \int g(\alpha_i, r)g(\alpha_j, r)\omega(r)r^2 dr. \quad (45)$$

Subtracting $\omega \times (44)$ from (43) ($\omega = \text{Constant}$), we have

$$F(D_1, \dots, D_n) = \sum_i \sum_j D_i D_j (O_{ij} - \omega S_{ij}) = \text{Max.}, \quad (46)$$

where $O_{ij} = P_i P_j$.

Differentiating F with respect to all D 's, and setting the results equal to 0, we have the secular equation

$$\sum_j (O_{ij} - \omega S_{ij}) D_j = 0. \quad i=1, N \quad (47)$$

By solving (47), we find D 's corresponding to maximum ω and F .

As in the wave function fitting, we vary α to get $\text{Max}(\omega_{\text{max}})$.

We then repeat the procedure for the expansion of V_{xc} .

Starting-matrix Calculation

The starting-matrix calculation is a very important step in the whole calculation. Without the right starting Hamiltonian matrix, the iteration would take longer computing time. Furthermore, it could be trapped at wrong points.

Since the solid is formed by bringing isolated atoms together, it is natural to begin with the atomic charge distribution,

$$\rho_0(\mathbf{r}) = \sum_m \rho_{\text{atom}}(\mathbf{r}-\mathbf{m}). \quad (48)$$

Notice that

$$V_{xc}(\mathbf{r}) = V_{xc}(\rho_0(\mathbf{r})^{1/3}) \quad (49)$$

is a non-linear function of the lattice sum of the charge density (48). (49) with (48) is called the overlapping-atomic-charge potential. So (49) will not equal the lattice sum of individual atomic potentials

The potential $V(r)$ consists of two parts (48, 50):

$$V_{xc}(r) = \sum_m v_{xc}(\rho(r-m)^{1/3}), \quad (50)$$

which is called the overlapping atomic potential. If we take the overlapping atomic potential as the starting potential for mathematical convenience, we have to compensate for that by adding a term equal to the difference between the overlapping-atomic-charge potential (50) and the overlapping atomic potential (49).

The starting matrix consists of four terms:

$$1) \langle a_i(r) | -1/2\nabla^2 | a_j(r-n) \rangle \quad (51)$$

$$2) \langle a_i(r) | [\sum_m v(r-m)] \exp(-r\gamma^2) | a_j(r-n) \rangle \quad (52)$$

$$3) \langle a_i(r) | [\sum_m v(r-m)] (1 - \exp(-r\gamma^2)) | a_j(r-n) \rangle \quad (53)$$

$$4) \langle a_i(r) | V_{xc}[\sum_m \rho(r-m)] - \sum_m v_{xc}[\rho(r-m)] | a_j(r-n) \rangle \quad (54)$$

where γ is chosen as 0.15.

All wave functions are expanded into Kubic-Harmonic-Gaussians

$$G(r) = g(r)K(x, y, z) \quad (55)$$

where K is a Kubic Harmonic [39], or linear combination of Spherical Harmonics, such as

$$S, X, Y, Z, 3Z^2-R^2, X^2-Y^2, XZ, YZ, XY.$$

The potential $V(r)$ consists of two parts (34,35,36): $-(Z/r)\exp(-r^2)$, which diverges at the origin, and a non-singular part, which is expanded into Gaussians.

Term 1 is the kinetic energy, term 2 is the screened overlapping atomic potential, term 3 is the difference between screened and unscreened potentials, and term 4 is the difference between the overlapping-atomic-charge potential and the overlapping atomic potential.

Before we go into calculation of Term 1 and 2, we would like first to examine how an integral, with two Gaussians located at different sites (called a two-center integral),

$$I = \int \exp(-\alpha r^2) \exp(-\beta(r-n)^2) d^3r, \quad (56)$$

can be done analytically.

This integral can be decomposed as the product of 3 terms with the same integrand form, that is, the product of three two-center integrals:

$$I = I_x \times I_y \times I_z, \quad (57)$$

where

$$I_x = \int \exp(-ax^2) \exp(-\beta(x-x_n)^2) dx, \quad (58)$$

and similar expressions hold for I_y and I_z .

It is not difficult to show that

$$\begin{aligned} I_x &= \exp[-(\alpha\beta/(\alpha+\beta))n_x^2] \int \exp(-(\alpha+\beta)(x-\beta n_x/\alpha+\beta)^2) dx \\ &= (\pi/\alpha)^{1/2} \exp[-(\alpha\beta/(\alpha+\beta))n_x^2], \end{aligned} \quad (59)$$

and similar results hold for I_y and I_z .

Thus a two-center integral is reduced to a one-center integral, which can be done in closed form. Similarly, a three-center integral, which is involved in term 2, can be reduced to two-center form, and then to one-center form.

The two- and three-center Gaussian integrals which include multiplicative polynomials (Kubic Harmonics are linear combinations of the polynomials), for example,

$$I = \int x \exp(-\alpha r^2) (y-y_n) \exp(-\beta(r-n)^2) d^3r, \quad (60)$$

can also be calculated in closed form [56-58].

The above conclusion is also valid for three-center integrals with the singular part of the potential at one of the centers [56-58]

$$I = \langle G_i(r) | \exp(-(r-m)^2) / |r-m| | G_j(r-n) \rangle. \quad (61)$$

The second derivative of G is a linear combination of polynomial-multiplied Gaussians:

$$\begin{aligned}
& \nabla^2 G(\mathbf{r}) \\
& = \nabla^2 g(\mathbf{r}) K_j(\mathbf{x}, \mathbf{y}, \mathbf{z}) \\
& = \sum_{\mathbf{l}} C_{\mathbf{l}} g(\mathbf{r}) P_{\mathbf{l}}(\mathbf{x}, \mathbf{y}, \mathbf{z}). \tag{62}
\end{aligned}$$

Then, since

$$a_i(\mathbf{r}) = \sum_{\mathbf{m}} D_{i,\mathbf{m}} G_{i,\mathbf{m}}(\mathbf{r}), \tag{63}$$

the kinetic energy term (51) may be written as

$$-(1/2) \sum_{\mathbf{m}} \sum_{\mathbf{n}} \sum_{\mathbf{l}} D_{i,\mathbf{m}} D_{j,\mathbf{n}} C_{\mathbf{l},\mathbf{j},\mathbf{n}} \langle G_{i,\mathbf{m}}(\mathbf{r}) | g_{\mathbf{n}}(\mathbf{r}-\mathbf{n}) P_{\mathbf{l},\mathbf{j},\mathbf{n}}(\mathbf{r}-\mathbf{n}) \rangle. \tag{64}$$

Once we know the integrals $\langle G_i(\mathbf{r}) | g(\mathbf{r}-\mathbf{n}) P_j(\mathbf{r}-\mathbf{n}) \rangle$, which are in fact worked out and tabulated [56-58], only algebraic manipulation is needed in order to calculate the kinetic energy term. No numerical integration is needed, which, in the case of very localized wave function, would be very time-consuming because a very fine mesh would be required to describe such wave functions.

The same is true for the potential energy calculation (52) except that a three-center-integral tabulation [56-58] is used and we need to sum over all atomic sites contributing to the potential. No numerical integration is involved in this case either. That is the reason why we expand the atomic wave function and atomic potential into Gaussians [59].

In the calculation of the potential term (52), we screened the atomic potential by multiplying it an exponential factor $\exp(-\gamma r^2)$, so that fewer atomic sites contribute to the overlapping atomic potential. But this screening effect is artificial. To include the difference between screened and unscreened potentials we use term 3 (53).

Term 3 is computed by Fourier Transformation. That is, in order to calculate

$$\delta V_{ij}(n) = \langle a_i(r) | \delta V(r) | a_j(r-n) \rangle, \quad (65)$$

we first calculate

$$\delta V(Q) = 1/V_{\text{cell}} \int_{\text{cell}} \delta V(r) \exp(-iQ \cdot r) d^3r \quad (66)$$

and

$$S_{ij}(n, Q) = \langle a_i(r) \exp(-iQ \cdot r) | a_j(r-n) \rangle. \quad (67)$$

Then, by summing over Q space, we get

$$\begin{aligned} \delta V_{ij}(n) \\ = \sum_Q \delta V(Q) S_{ij}(n, Q). \end{aligned} \quad (68)$$

$S_{ij}(n, Q)$ is also a kind of two-center integral, and it can be integrated in closed form [58].

Since $\delta V(r)$ is a slowly varying function in real space, $\delta V(Q)$ will vanish at large Q (large Q means rapid

oscillation in the integrand, leading to phase cancellation). It is this slowly varying property which makes it possible to expand $\delta V(r)$ into plane waves with only a modest number of Q's:

$$\begin{aligned}
 \delta V(Q) &= 1/V_{\text{cell}} \int_{\text{cell}} \left[\sum_{m=-\infty}^{\infty} \delta v(r-m) \right] \exp(-iQ \cdot r) d^3r \\
 &= 1/V_{\text{cell}} \int_{\infty} \left[\sum_{m=\text{cell}} \delta v(r-m) \right] \exp(-iQ \cdot r) d^3r \\
 &= 1/V_{\text{cell}} \int_{\infty} \left[\sum_{m=\text{cell}} \exp(-iQ \cdot m) \right] \int_{\infty} \delta v(r-m) \exp(-iQ \cdot (r-m)) d^3r \\
 &= 1/V_{\text{cell}} \int_{\infty} \left[\sum_{m=\text{cell}} \exp(-iQ \cdot m) \right] \int_{\infty} \delta v(r) \exp(-iQ \cdot r) d^3r \quad (69)
 \end{aligned}$$

Now $\int \delta v(r) \exp(-iQ \cdot r) d^3r$ is independent of lattice site m , and can be reduced to a one-dimensional numerical integration:

$$\begin{aligned}
 &\int_{\infty} \delta v(r) \exp(-iQ \cdot r) d^3r \\
 &= (2/Q) \int_0^{\infty} V_{\text{atomic}}(r) (1 - \exp(-\gamma r^2)) \sin(Qr) r dr. \quad (70)
 \end{aligned}$$

We also apply the Fourier transformation technique to term 4 (54). In this case, we have to perform a three-dimensional numerical integration to calculate

$$\delta V'(Q) = 1/V_{\text{cell}} \int_{\text{cell}} \delta V'(r) \exp(-iQ \cdot r) d^3r. \quad (71)$$

Fortunately, $\delta V'(r)$, the difference between the overlapping-atomic-charge potential (49) and the

overlapping atomic potential (50), is also slowly varying. Although near the nucleus, both atomic charge and atomic potential have their maximum value and change most rapidly, very little atomic charge overlaps there, which makes $\delta V'(r)$ small. In fact, $\delta V'(r)$ has its largest contribution in the interstitial region where it varies slowly. As the result of this slowly varying nature, we only need to include modest numbers of mesh points, both in real space and reciprocal space for the integrations.

Here we would like to point out that in our matrix element calculation, we did not use the nearest-neighbor approximation, as is often used by other workers. We calculate the matrix element $\langle a_i(r) | H(r) | a_j(r-n) \rangle$ for any i, j, n as small as 10^{-6} (The largest matrix element is of order 10^{+2} , for comparison), no matter how far apart

the atoms are. In fact, we calculate up to 15th nearest neighbors ($|n|=27$ a.u.) for the most diffuse 5s atomic wavefunctions located at the same lattice plane.

Finally, we want to discuss the relation between the number of points in real space and Q space [60]. For simplicity, we only consider the one-dimensional case. The generalization to the three-dimensional case is obvious.

A periodic function in real space with period X can be expanded into a Fourier series as

$$f(x) = \sum_n F(n) \exp(-i2\pi nx/X), \quad (72)$$

where

$$F(n) = (1/X) \int_0^X f(x) \exp(i2\pi nx/X) dx, \quad (73)$$

for $f(x)$ given at continuous x . If, on the other hand, $f(x)$ is given only at discrete x values, as is always true in numerical calculation by computer, $F(n)$ will be changed from an integral to a summation:

$$F(n) = (1/N) \sum_{j=1}^N f((j-1/2)\Delta x) \exp(i2\pi(j-1/2)n/N) \quad (74)$$

where $f(x)$ is sampled at N equally spaced points, and $x_1 = 0.5 \Delta x$, as in our numerical integration.

It is easy to show that

$$F(n+N) = -F(n), \quad \text{for } n=1, N \quad (75)$$

that is, there are only N F 's which are distinct. Thus the number of points in real space equals the number of points in reciprocal space. If the information in the real space is limited, we can not gain more insight by using more points in the reciprocal space.

Symmetry

Here we would like to discuss the symmetry properties of the system. Without using the symmetry, the calculation would be much more time-consuming.

First of all, there is a translation symmetry of the potential in the XY plane, that is, $V(\mathbf{r}+\mathbf{R})=V(\mathbf{r})$, where \mathbf{R} is any lattice-displacement vector in the plane. Thus, we only need to consider one unit cell. Every physically observable quantity behaves exactly the same in any other cell. The wave function in different cells, however, obeys the Bloch condition: $\Psi_{\mathbf{k}}(\mathbf{r}+\mathbf{R})=\exp(-i\mathbf{k}\cdot\mathbf{R})\Psi_{\mathbf{k}}(\mathbf{r})$. Thus we need to introduce a good quantum number, the 2-dimensional \mathbf{k} vector, to represent the wave function. The basis then is \mathbf{k} dependent. The Hamiltonian matrix is block-diagonal in \mathbf{k} . The number of \mathbf{k} vectors, in principle, is infinite for the system with infinite extension. Fortunately, only a few of them (6 special \mathbf{k} points [61] in the irreducible wedge of the surface Brillouin zone (IBZ), or 36 in the whole first surface Brillouin zone), according to our tests, are necessary to iterate to self-consistency, and 45 \mathbf{k} points in the IBZ are needed for the last iteration, based on which we can interpolate the energy and wave function for other \mathbf{k} 's. On the other hand, the introduction of \mathbf{k} makes the effective Hamiltonian [62]

lose its C_{4v} symmetry for a general k point, and this makes diagonalization more difficult.

In the Z direction, there is no translation symmetry, due to the existence of the surface. The unit cell has to include all layers of the slab. That is the reason why we need atomic basis function for every layer, as mentioned above. What we have now for our model is one slab with vacuum at both sides. However, in order to perform the three-dimensional Fourier transformation to calculate charge density and therefore potential, we must repeat the slab in the Z direction. The space between slabs is so large (~ 100 a.u. compared with ~ 5 a.u. between nearest neighbors) that there is no interaction at all between slabs. There is no need to introduce a k vector in the Z direction, or equivalently, there is no $E(k_z)$ dispersion, so we only need to consider $k_z=0$.

The point group of the Hamiltonian of the (100) surface for F.C.C. or B.C.C. crystalline structures is $C_{4v} \times R = D_{4h}$.

The C_{4v} group has 8 symmetry operations and 5 classes. They are:

	E	C_2	C_4	C_4'	σ_h	σ_v	σ_d	σ_d'	
X	X	-X	Y	-Y	X	-X	Y	-Y	
Y	Y	-Y	-X	X	-Y	Y	X	-X	(76)

The R group has 2 symmetry operations. They are:

$$\begin{array}{ccc}
 & E & \sigma_z \\
 Z & Z & -Z
 \end{array} \quad (77)$$

Because of the C_{4v} symmetry of $V(r)$, k 's in the IBZ would be sufficient to represent all k 's involved in V_{eff} in the whole first BZ. For any k which is in the BZ but not in the IBZ we can always perform some kind of C_{4v} operation to place it in the IBZ without changing the physical situation. The only things changed are the XY coordinate which is indeed arbitrary within a 90-degree rotation, and right-left-hand-coordinate convention.

For the effective Hamiltonian $H=E_k+V(r)+K \cdot p$ [62], the C_{4v} symmetry is retained only at Γ and M.

At X the symmetry for V_{eff} is C_{2v} , which has 4 operations and 4 classes. They are:

$$\begin{array}{ccccc}
 & E & C_2 & \sigma_h & \sigma_v \\
 X & X & -X & X & -X \\
 Y & Y & -Y & -Y & Y
 \end{array} \quad (78)$$

At Δ , Σ and Y, the symmetry is reduced to E and σ_h (for Δ) or σ_v (for Y) or σ_d (for Σ):

$$\begin{array}{ccc}
 & E & \sigma_h \\
 X & X & X \\
 Y & Y & -Y
 \end{array} \quad (79)$$

$$\begin{array}{ccc}
 & E & \sigma_v \\
 X & X & -X \\
 Y & Y & Y
 \end{array} \tag{80}$$

$$\begin{array}{ccc}
 & E & \sigma_d \\
 X & X & Y \\
 Y & Y & X
 \end{array} \tag{81}$$

At a general k point, however, there is no point group operation which will leave the effective Hamiltonian invariant. So the only symmetry left is the Z reflection symmetry, which leads us to make even and odd linear combinations of atomic wave functions located at opposite sides of the slab. There is no coupling between these even and odd functions, thus reducing the dimension of the matrix by a factor of 2.

The atomic orbitals belonging to the different representation of the group of the wave vector [62] is shown in Table 1.

Table 1 Atomic Wave Function and Point Group Representation

Point Group	Atomic Wave Function	
	Site(0,0)	Site(c/2, c/2)
Γ_1	$S, Z, 3Z^2 - R^2$	$S, Z, 3Z^2 - R^2$
Γ_2	NULL	NULL
Γ_3	$X^2 - Y^2$	$X^2 - Y^2$
Γ_4	XY	XY
Γ_5	(X, Y) (XZ, YZ)	(X, Y) (XZ, YZ)
M_1	$S, Z, 3Z^2 - R^2$	XY
M_2	NULL	$X^2 - Y^2$
M_3	$X^2 - Y^2$	NULL
M_4	XY	$S, Z, 3Z^2 - R^2$
M_5	(X, Y) (XZ, YZ)	(X, Y) (XZ, YZ)
X_1	$S, Z, X^2 - Y^2, 3Z^2 - R^2$	X, XZ
X_2	XY	Y, YZ
X_3	X, XZ	$S, Z, X^2 - Y^2, 3Z^2 - R^2$
X_4	Y, YZ	XY
Δ_1	$S, X, Z, XZ, X^2 - Y^2, 3Z^2 - R^2$	$S, X, Z, XZ, X^2 - Y^2, 3Z^2 - R^2$
Δ_2	Y, XY, YZ	Y, XY, YZ
Y_1	$S, Y, YZ, X^2 - Y^2, 3Z^2 - R^2$	X, XY, XZ
Y_2	X, XY, XZ	$S, Y, YZ, X^2 - Y^2, 3Z^2 - R^2$
Σ_1	$S, X+Y, Z, XY, XZ+YZ, 3Z^2 - R^2$	$S, X+Y, Z, XY, XZ+YZ, 3Z^2 - R^2$
Σ_2	$X-Y, XZ-YZ, X^2 - Y^2$	$X-Y, XZ-YZ, X^2 - Y^2$

In the irreducible wedge of the first BZ, $[\Delta X Y M \Sigma]$, the knowledge of [76],[77-81] and Table 1 helps us to identify the atomic orbitals involved in any energy level. Furthermore, the band structure can be interpolated between calculated eigenvalues having the same symmetry properties. These interpolated energy bands can then be compared directly with the experimental data obtained from angle-resolved-photoemission spectroscopy.

The Hamiltonian of the system is invariant under all operations of the point group D_{4v} . This fact is applied in the starting-matrix-element calculation. We only need to calculate

$$H_{ij}(n) = \langle a_i(r) | H(r) | a_j(r-n) \rangle \quad (82)$$

for n in $1/8$ of the plane. Then by applying the C_{4v} symmetry of $V(r)$, we can obtain $H_{ij}(n)$ for n in all other parts of the plane. Furthermore, once we know $\langle a_i(r-m) | H(r) | a_j(r-n) \rangle$ for some $n-m$ (Here we changed the origin of the coordinate from the atom where a_i is located to the atom in the central layer), we can easily obtain the corresponding matrix element for $(n'-m')_z = -(n-m)_z$ with $m'_z = -m_z$ and $(n'-m')_{\parallel} = (n-m)_{\parallel}$ by applying the Z-reflection symmetry of $H(r)$. The procedure is the following:

Define

$$H_{ij}(n) = \langle a_i(r) | H(r) | a_j(r-n) \rangle. \quad (83)$$

Performing a C_{4v} operation on r 's, we have

$$H_{ij}(an) = \langle a_i(ar) | H(ar) | a_j(a(r-n)) \rangle. \quad (84)$$

By C_{4v} symmetry of the Hamiltonian, we have

$$H(ar) = H(r). \quad (85)$$

$a_i(a(r-n))$ can be expanded as

$$a_i(a(r-n)) = \sum_p D_{pi}(a) a_p(r-n). \quad (86)$$

So

$$\begin{aligned} & H_{ij}(an) \\ &= \langle \sum_p D_{pi} a_p(r) | H(r) | \sum_q D_{qj} a_q(r-n) \rangle \\ &= \sum_p \sum_q D_{pi}^* D_{qj} H_{pq}(n) \\ &= \sum_p \sum_q (D_{ip})^+ H_{pq}(n) D_{qj}. \end{aligned} \quad (87)$$

In matrix form,

$$H' = D^+ H D. \quad (88)$$

Thus, once we know the transformation properties of the wave function (86), we can easily obtain the transformation properties of matrix elements. By rotating or reflecting the lattice site n involved in the matrix element, the calculated results for lattice site n in the

1/8 of the XY plane can be generalized into the whole plane with only some algebraic manipulation.

An example of this transformation is given in Fig.3.

The coefficients $D(\alpha)$ for all C_{4v} elements α can be easily worked out by applying (76) to all atomic wave functions. Table 2 gives D 's for C_4 and σ_v . For all other operations, the D matrix can be obtained by multiplication of the D 's already known. Thus,

$$C_2 = C_4 \times C_4, \quad (89)$$

$$C_4^3 = C_4 \times C_4 \times C_4, \quad (90)$$

$$E = C_2 \times C_2, \quad (91)$$

$$\sigma_h = C_2 \times \sigma_v, \quad (92)$$

$$\sigma_d = C_4 \times \sigma_h, \quad (93)$$

$$\sigma_d^3 = C_2 \times \sigma_d. \quad (94)$$

A similar argument allows one to apply reflection symmetry $H(-z) = H(z)$ to get $\langle a_i(r-m') | H(r) | a_j(r-n') \rangle$ once we know $\langle a_i(r-m) | H(r) | a_j(r-n) \rangle$ with $(n'-m')_z = -(n-m)_z$, $m'_z = -m_z$ and $(n'-m')_{\parallel} = (n-m)_{\parallel}$. $D(\sigma_z)$ is shown in Table 3.

An example of this transformation is given in Fig.4.

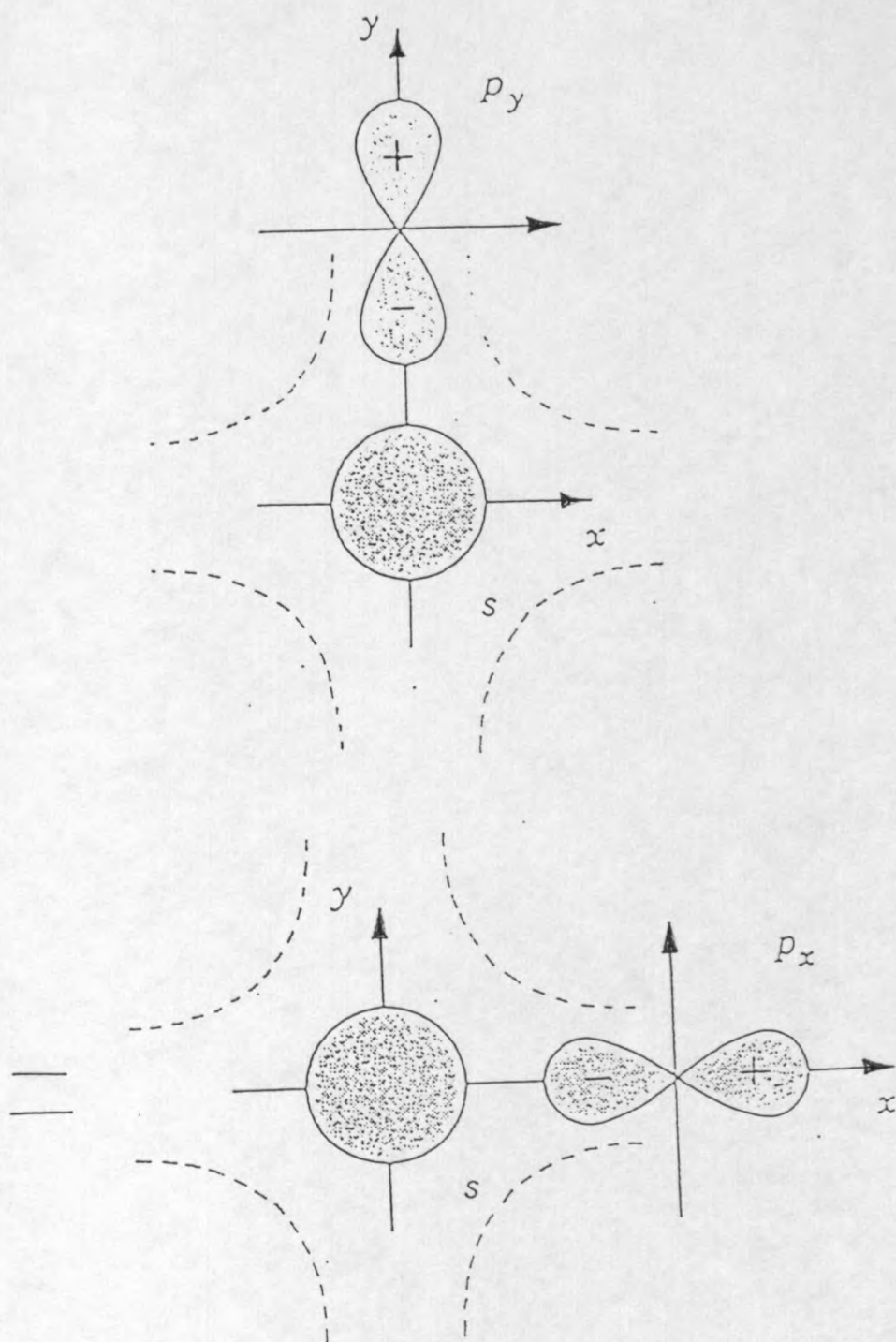


Fig.3 Application of C_{4v} symmetry of the crystal potential in the matrix-element calculation. $\langle s(\mathbf{r}) | H(\mathbf{r}) | p_y(\mathbf{r}-\mathbf{n}) \rangle = \langle s(\mathbf{r}) | H(\mathbf{r}) | p_x(\mathbf{r}-\mathbf{n}') \rangle$, where $\mathbf{n}=(0, a)$ and $\mathbf{n}'=(a, 0)$. Dashed lines represent a C_{4v} -symmetric potential.

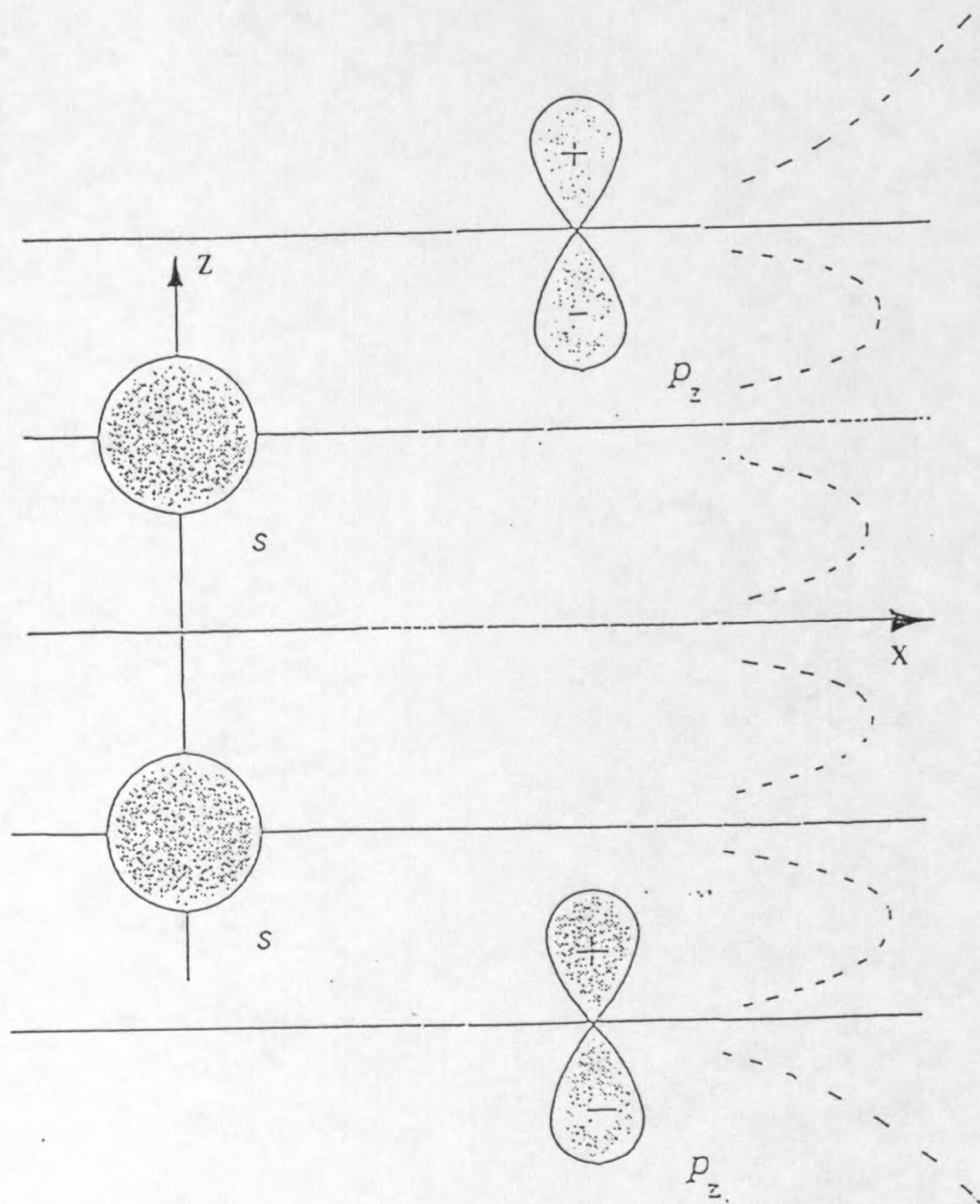


Fig.4 Application of Z-reflection symmetry of the crystal potential in the matrix-element calculation. $\langle s(r-m) | H(r) | p_z(r-n) \rangle = -\langle s(r-m') | H(r) | p_z(r-n') \rangle$, where $m_z = a/2$, $n_z = a$, $m'_z = -a/2$, and $n'_z = -a$. Dashed lines represent an R-symmetric potential.

There is one more symmetry in real space which is useful. For two atomic orbitals located in the same layer or the opposite layer from the center of the slab, we have

$$\begin{aligned}
 H_{ij}(n) &= \langle a_i(r) | H(r) | a_j(r-n) \rangle \\
 &= \langle a_i(r+n) | H(r+n) | a_j(r) \rangle \\
 &= \langle a_j(r) | H(r) | a_i(r+n) \rangle^* \\
 &= H_{ij}(-n)^* \tag{95}
 \end{aligned}$$

provided $H(r+n)=H(r)$ is true. This is indeed valid in the case mentioned above.

The inversion of lattice site n might change the sign of the matrix element. That is

$$H_{ij}(-n) = \pm H_{ij}(n). \tag{96}$$

Notice $I=C_2x\sigma_z$. So by (87) we can determine whether the sign will change or not.

The complex conjugate might also lead to a sign change. That is,

$$H_{ij}(n)^* = \pm H_{ij}(n). \tag{97}$$

In fact, we changed the basis orbitals p_x, p_y, d_{xz}, d_{yz} by multiplying each of them by i to make the lattice sum $H_{ij}(k)$ real and symmetric. Depending on the number of

imaginary basis orbitals involved (1 or 2), the matrix element will (will not) go to its negative value when we complex-conjugate it. Combining the two possible minus signs, $H_{ji}(n)$ may be obtained from $H_{ij}(n)$. In other words, we only need to calculate the matrix element with $i \rangle j$ for atomic wave functions located on the same plane or on planes situated on the opposite sides of the central plane.

When the lattice sum of the Hamiltonian

$$\begin{aligned} H_{ij}(k) &= \sum_m \exp(-ik \cdot m) \langle a_i(r) | H(r) | a_j(r-m) \rangle \\ &= \sum_m [\cos(k \cdot m) - i \sin(k \cdot m)] H_{ij}(m) \end{aligned} \quad (98)$$

is performed, we would have imaginary $H_{ij}(k)$ due to the sin term above unless $H_{ij}(m)$ is imaginary. This can be done if the basis functions with odd symmetry under the planar inversion C_2 , p_x , p_y , d_{xz} , and d_{yz} are each multiplied by i . Then when one imaginary function is involved in $H_{ij}(m)$, $H_{ij}(m)$ will be imaginary, and furthermore, it is easy to show that $H_{ij}(-m) = -H_{ij}(m)$. Thus the sin term will be real, while the cos term will vanish after summation over m . On the other hand, when none or two imaginary functions are involved in $H_{ij}(m)$, it can be shown that the sin term, which is imaginary, will vanish after summation over m since $H_{ij}(-m) = H_{ij}(m)$ in this case.

As the result, the lattice sum $H_{ij}(k)$ is real. The same is true for $O_{ij}(k)$.

In addition to D_{4h} symmetry in real space, there is also a D_{4h} symmetry in Q space, that is, the reciprocal space of Fourier transformation.

$$V(Q) = 1/V_{\text{cell}} \int V(r) \exp(-iQ \cdot r) d^3r. \quad (99)$$

Performing a symmetry operation R of D_{4h} on $V(Q)$, we have

$$V(RQ) = 1/V_{\text{cell}} \int V(r) \exp(-iRQ \cdot r) d^3r \quad (100)$$

Noticing

$$RQ \cdot r = R^{-1}RQ \cdot R^{-1}r = Q \cdot R^{-1}r, \quad (101)$$

we have

$$V(RQ) = 1/V_{\text{cell}} \int V(r) \exp(-iQ \cdot R^{-1}r) d^3r \quad (102)$$

Due to the D_{4h} symmetry in real space:

$$V(R^{-1}r) = V(r), \quad (103)$$

we have

$$V(RQ) = 1/V_{\text{cell}} \int V(r') \exp(-iQ \cdot r') d^3r' = V(Q) \quad (104)$$

where $r' = R^{-1}r$.

Thus we not only have D_{4h} symmetry in real space, but also in Q space. Only those $V(Q)$'s with Q_{xy} in the $1/8$ of the Q_{xy} plane and with $Q_z > 0$ are needed in the calculation.

Self-consistent Iteration

Define

$$V(\mathbf{r}) = F(\mathbf{r}) + V_{xc}(\mathbf{r}) \quad (105)$$

where $F(\mathbf{r}) = \int \rho(\mathbf{r}') / |\mathbf{r} - \mathbf{r}'| d^3r$ is the electrostatic potential between electrons, and it is non-local.

Also define

$$\delta V(\mathbf{r}) = V(\mathbf{r}) - V_0(\mathbf{r}), \quad (106)$$

$$\delta F(\mathbf{r}) = F(\mathbf{r}) - F_0(\mathbf{r}), \quad (107)$$

$$\delta V_{xc}(\mathbf{r}) = V_{xc}(\mathbf{r}) - V_{xc0}(\mathbf{r}), \quad (108)$$

$$\delta \rho(\mathbf{r}) = \rho(\mathbf{r}) - \rho_0(\mathbf{r}), \quad (109)$$

where $V_0(\mathbf{r})$ ($F_0(\mathbf{r}), V_{xc0}(\mathbf{r})$) is the overlapping-atomic-charge total (electrostatic, exchange-correlation) potential, and $\rho_0(\mathbf{r})$ is the overlapping atomic charge density. They do not change during the iteration.

The Fourier transforms of $\delta \rho(\mathbf{r})$ and $\delta V_{xc}(\mathbf{r})$ are:

$$\delta \rho(Q) = 1/V_{cell} \int \delta \rho(\mathbf{r}) \exp(-iQ \cdot \mathbf{r}) d^3r, \quad (110)$$

$$\delta V_{xc}(Q) = 1/V_{cell} \int \delta V_{xc}(\mathbf{r}) \exp(-iQ \cdot \mathbf{r}) d^3r. \quad (111)$$

Although $\rho(r)$ and $V_{xc}(r)$ are not quite slowly varying functions over all space, $\delta\rho(r)$ and $\delta V_{xc}(r)$ are. Near the atomic nucleus where the charge is dense and the potential is deep, the electrons are so strongly affected by the nearby nucleus that they hardly feel the existence of other atoms. In other words, $\delta\rho(r)$ and $\delta V_{xc}(r)$ are practically zero in this region (called the core region). Thus we can freeze the charge density contributed from iron atomic 1s, 2s, 2p, 3s, 3p-like states and oxygen atomic 1s-like states at their free atomic values, as well as the corresponding exchange-correlation potential. This is called the frozen-core approximation. It is not necessary, as we demonstrated above, nor possible, to treat the core electrons self-consistently unless a very large number of mesh points, up to 10^3 as many as we are using now, are used both in real space and reciprocal space, and furthermore, unless the LDA formulation is improved so that it is applicable even in the region where the potential as well as the charge density vary rapidly. Recall that the LDA is derived for homogeneous systems. In other words, the LDA will break down in the core region. In the interstitial region and surface region, on the other hand, both $\rho(r)$ and $V_{xc}(r)$ are altered appreciably from their free atomic values. That is, charge rearrangement occurs due to the formation of the solid

from isolated atoms. This charge rearrangement $\delta\rho(r)$, the difference between $\rho(r)$ and $\rho_0(r)$, varies slowly in space. This is also true for $\delta V_{xc}(r)$ in (109). Thus in Fourier transformations (110) and (111), we only need a modest number of real-space and reciprocal-space points.

Although the electrostatic potential

$$F(r) = \int \rho(r') / |r-r'| d^3r \quad (112)$$

is non-local in real space, the Fourier transform of it

$$F(Q) = \rho(Q) / (4\pi Q^2) \quad (113)$$

is local in Q space, and it is easy to calculate $\delta F(Q)$ once we know $\delta\rho(Q)$, except for the $Q=0$ component, where both numerator and denominator are zero. In this case, a limiting procedure is used. Instead of $Q=0$, we use $Q_x=0$, $Q_y=0$ and $Q_z=10^{-4}$ (compared to the next-smallest Q vector: $Q_x=0$, $Q_y=0$ and $Q_z=0.1$).

Once we know $\delta F(Q)$ and $\delta V_{xc}(Q)$, we obtain $\delta V(Q)$ by (105). We give $\delta V(Q)$ a subscript and superscript, so it is now written as $\delta V(Q)_n^{\text{out}}$, to indicate this is the output potential of the n th iteration. Then we construct

$\delta V(Q)_{n+1}^{\text{in}}$, the input potential for the next iteration:

$$\delta V(Q)_{n+1}^{\text{in}} = \delta V(Q)_n^{\text{in}} + \alpha (\delta V(Q)_n^{\text{out}} - \delta V(Q)_n^{\text{in}}), \quad (114)$$

where α is a convergence factor ranging from 0.01 to 0.1

(instead of 1, in which case the output from an iteration would be the input of the next iteration) to prevent overcompensation by the iterating correction.

$\delta V(Q)_i^{in}$, the input potential difference for the first iteration, is zero by definition.

After calculation in Q space, we sum over all Q points to get

$$\delta H_{ij}(n) = \sum_Q \alpha (\delta V_n^{out}(Q) - \delta V_n^{in}(Q)) \times S_{ij}(n, Q), \quad (115)$$

where

$$S_{ij}(n, Q) = \langle a_i(r) | \exp(-iQ \cdot r) | a_j(r-n) \rangle, \quad (116)$$

which was calculated and stored when we were calculating the starting matrix element.

Then we use this correction to construct a new Hamiltonian, obtaining

$$H_{ij}(n)_{n+1} = H_{ij}(n)_n + \delta H_{ij}(n)_n. \quad (117)$$

This is equivalent to the convergence technique (114) in Q space.

We then begin another iteration until

$$\delta H_{ij}(0)/\alpha < 0.1 \text{ eV} \quad (118)$$

for all $i, j = (\text{Fe})3d, 3d$ and $(O)2p, 2p$ orbitals. This is the criterion for convergence. This on-site matrix-element

correction is a kind of average energy correction for Fe 3d-like and O 2p-like levels. 0.1eV, the theoretical uncertainty, is about the same order as the corresponding experimental error.

In the $\delta\rho(Q)$ calculation, we mentioned that for the $Q=0$ component, $\delta\rho(Q)$ has to vanish, otherwise $\delta F(Q)$ would diverge. That is,

$$\delta\rho(Q=0) = 1/V_{\text{cell}} \int (\rho(\mathbf{r}) - \rho_0(\mathbf{r})) d^3\mathbf{r} = 0, \quad (119)$$

or the total charge during the iteration has to be equal to the total overlapping atomic charge. Unfortunately, due to the finite mesh size, these two integrals are never equal. So we normalize both of them to their ideal value: the number of valence electrons per unit cell. The normalization factor never deviates from 1 by as much as 0.02. In fact, this 0.02 deviation is the criterion for judging the proper size of the real space mesh. In the calculation, the mesh size used is one twelfth of the lattice constant 0.45 a.u. to guarantee proper integrated total charge.

We now explain how the spin-polarized iteration is done. At the start of the iteration procedure, we assume the system is paramagnetic, that is, there is no spin-dependence of the electronic structure of the system. We continue to iterate as we described above until close to

convergence under the artificial restriction of paramagnetism. Then we introduce a perturbation:

For majority-spin energy levels, let

$$E_{\uparrow} = E - \delta E. \quad (120)$$

For minority-spin energy levels, let

$$E_{\downarrow} = E + \delta E, \quad (121)$$

where δE is a positive number and is the estimated value of the final self-consistent spin splitting. Thus we introduce ferromagnetism artificially, to break the symmetry of the paramagnetic state. Since the energy levels are rigidly shifted, some are lowered creating extra occupied states (compared to the paramagnetic case) to form the majority-spin distribution, while others are raised creating extra empty states to form the minority-spin distribution. As a result, we get a correction to the Hamiltonian for both spins. From the next iteration on, we diagonalize the Hamiltonian for spin_{\uparrow} and spin_{\downarrow} separately. This spin splitting is not self-consistent yet. So we keep on iterating until self-consistency is reached, that is, until (118) is valid for each spin.

Lowdin Representation

In order to interpret the calculated eigenfunctions, we have to go back to examine our basis (22). The orthonormality condition, though valid in many cases in quantum mechanics, is not valid here:

$$\begin{aligned} & \langle F_i(r, k) | F_j(r, k) \rangle \\ & \sim \sum_m \exp(-ik \cdot m) \langle a_i(r) | a_j(r-m) \rangle \\ & \neq \delta_{ij}, \end{aligned} \tag{122}$$

because the off-site atomic wave functions do not obey the orthonormality condition

$$\langle a_i(r) | a_j(r-m) \rangle = \delta_{ij} \tag{123}$$

unless there is a symmetry reason or the two atoms are so far apart that there is no overlap between their atomic wave functions.

The overlap of the atomic wavefunctions plays an essential role in solid state physics. If there were no overlap, there would be no interaction between atoms. Then the solid would be a free atomic gas. All properties would be exactly the same as for isolated atoms. Non-orthonormality is intrinsic in solid state physics.

But, with this non-orthonormal basis set, it is difficult to interpret the components of an eigenfunction, namely, the C's in (23). The square of C_i would be the occupation probability for a given eigenstate of the i th atomic Bloch orbital in the orthonormal-basis-set case. But the meaning of the C's is not clear in the general case.

Mulliken [63] proposed that the C's should be normalized to unity by

$$\sum_i \sum_j C_i O_{ij} C_j = 1 \quad (124)$$

and that

$$C_i \sum_j O_{ij} C_j = P_i \quad (125)$$

be interpreted as the occupation probability of the i th atomic Bloch orbital for a given eigenstate.

During the iteration, we do not need to interpret the C's, but we do use (124) to normalize the C's to unity.

Another projection technique, proposed by Lowdin [64], is to first make the basis set orthonormal, and then to follow the usual interpretation: the squares of the C's are occupation probabilities. In making the basis set orthonormal, we are actually taking linear combinations of the old basis functions to form new basis functions. In this way, the basis functions are no longer pure atomic

Bloch orbitals centered at certain layers. They are all mixed up as long as symmetry does not prevent mixing.

The Lowdin representation is derived as follows. The matrix form of the Schrodinger equation is

$$HC=EOC. \quad (126)$$

A unitary matrix M which diagonalizes O and its complex conjugate M^+ are applied to the equation to obtain

$$M^+HMM^+C=EM^+OMM^+C, \quad (127)$$

where

$$M^+OM=O', \quad (128)$$

is a diagonal, positive-definite matrix.

Define

$$H'=M^+HM \quad (129)$$

and

$$C'=M^+C. \quad (130)$$

Then the Schrodinger equation (126) becomes

$$H'C'=EO'C'. \quad (131)$$

The corresponding basis functions are already orthogonal, but not normalized yet.

Since O' is positive definite, we can define two matrices from O' :

$$O'_{i,i}{}^{1/2} = (O'_{i,i})^{1/2} \quad (132)$$

and

$$O'_{i,i}{}^{-1/2} = 1/(O'_{i,i}{}^{1/2}). \quad (133)$$

Multiply (131) by (132) and (133) as follows:

$$\begin{aligned} & O'_{i,i}{}^{-1/2} H' O'_{i,i}{}^{-1/2} O'_{i,i}{}^{1/2} C' \\ &= E O'_{i,i}{}^{-1/2} O'_{i,i}{}^{-1/2} O'_{i,i}{}^{1/2} C' \\ &= E O'_{i,i}{}^{1/2} C'. \end{aligned} \quad (134)$$

Define

$$H'' = O'_{i,i}{}^{-1/2} H' O'_{i,i}{}^{-1/2} \quad (135)$$

and

$$C'' = O'_{i,i}{}^{1/2} C'. \quad (136)$$

The Schrodinger equation (126) becomes

$$H'' C'' = E C''. \quad (137)$$

The basis set now is orthonormal, so the components of the eigenfunction should be easy to interpret if the basis functions themselves have definite physical meaning. Unfortunately, this is not the case. When $C \rightarrow C' \rightarrow C''$, the basis functions are mixed at general k points, except that even and odd functions (with respect to the Z reflection) will not be transformed into each other.

Nevertheless, the 3d atomic wavefunctions are not too expanded. In the Lowdin transformation they do not mix much with other basis functions. So it is still meaningful to talk about occupation numbers of 3d levels using our new basis set.

We use 6 k points in the IBZ for iteration. A trial calculation showed there is essentially no change when 15 k points are used. Perhaps this is because the Fe density of states is not too large at the Fermi energy. However, for the last iteration, we use 45 k points in the IBZ in order to

- 1) interpolate the k dependence of eigenenergies and eigenfunctions of the Schrodinger equation for about 10000 randomly generated k points, to get a smooth density of states (DOS).

- 2) draw energy bands along high-symmetry lines (this is also a kind of interpolation) which can be compared directly to the ARPES.

We discussed 2) in detail in the section on Symmetry. Here we focus on the DOS calculation.

We use a Monte Carlo technique to select 10000 k points scattered randomly and uniformly in the first BZ. For each k point chosen, we quadratically interpolate both the energy and occupation number of all Lowdin orbitals, which are labeled by the 'atomic' wave function and the layer to which the 'atomic' wave function belongs, from previous self-consistent calculations of the nearest k points.

After the interpolation, we begin to count levels to obtain the density of states

$$N(E) = \sum_j \sum_k \delta(E - E_j(k)) \quad (138)$$

where

$$\delta(E - E_j(k)) = 1, \quad \text{for } E < E_j(k) < E + 0.001(\text{Hartree}) \quad (139)$$

$$\delta(E - E_j(k)) = 0, \quad \text{for } E \text{ otherwise} \quad (140)$$

and E itself is 0.001 Hartree spaced. Thus a histogram is generated by counting all energy values falling within the specified intervals. A five-point-weighting-average technique is used to remove statistical noise of DOS.

The orbital-layer-projected DOS for the *i*th orbital and *l*th layer is defined as

$$N_o(E, i, l) = \sum_j \sum_k C_{i, l}(j, k)^2 \delta(E - E_j(k)) \quad (141)$$

The layer-projected DOS for the l th layer is defined as

$$N_1(E, l) = \sum_i N_o(E, i, l) \\ = \sum_j \sum_k \sum_i C_{i, l}(j, k)^2 \delta(E - E_j(k)) \quad (142)$$

The occupation number is defined as the summation (or integration) of the DOS up to Fermi energy. The possible indices i, l or l are omitted.

$$n = \sum_{E < E_F} N(E) \quad (143)$$

The definitions above, (138), (141)---(143), in fact, are implied for a particular spin only. Now we have to indicate a spin dependence explicitly.

The total occupation number is defined as:

$$n = n_{\uparrow} + n_{\downarrow}, \quad (144)$$

and the magnetic moment is defined as:

$$m = n_{\uparrow} - n_{\downarrow}, \quad (145)$$

in both cases the possible indices i, l or l are omitted.

These DOS, especially orbital-layer-projected DOS N_o and layer-projected DOS N_1 , will turn out to be very useful in developing insight into bonding mechanisms, charge transfer between layers, and magnetic moment variations from the surface to the center layer. We will discuss these in detail in Chapter 3.

Finally, we would like to define layer occupation probability on a layer l for a given eigenstate as:

$$p(l, j, k) = \sum_i C_{i, l}(j, k)^2 \quad (146)$$

where i sums over all atomic Block orbitals located at the layer l . This $p(l, j, k)$ tells us how much $\psi_j(k)$ is localized on a certain layer l . In particular, those states with $p(\text{surface}) > 60\%$ are defined as the surface states. We will discuss surface-state bands in detail in Chapter 3.

CHAPTER 3

RESULTS AND DISCUSSIONS

Two-Level Bonding Model

Before going to the detailed discussion of the calculated results, we would like to first examine a simple calculation for a two-level bonding model. Although the slab calculation we performed is much more sophisticated, the basic physics is the same as in the simple two-level model calculation. We emphasize that we did not use this two-level model in our slab calculation. Yet the model can be used to interpret the results of the slab calculation, to see what kind of physical processes are going on, and to see whether or not the slab calculation agrees qualitatively with our simple, intuitive thinking based on the two-level problem.

The two-level Schrodinger matrix equation with basis functions ϕ_1 and ϕ_2 can be written as follows:

$$\begin{pmatrix} H_{11}-E & H_{12} \\ H_{21} & H_{22}-E \end{pmatrix} \begin{pmatrix} C_1 \\ C_2 \end{pmatrix} = 0 \quad (147)$$

where $H_{21}^* = H_{12}$ by the Hermitian property of the Hamiltonian.

By solving (147), we get

$$E = (1/2) \times [(H_{11} + H_{22}) \pm ((H_{11} - H_{22})^2 + 4H_{12}^2)^{1/2}] \quad (148)$$

and the corresponding two eigenfunctions.

If there is no coupling between the two levels,

$$H_{12} = 0, \quad (149)$$

then

$$E_1 = H_{11} \quad \text{and} \quad E_2 = H_{22}. \quad (150)$$

The two eigenfunctions are simply pure ϕ_1 and ϕ_2 .

In the case of weak coupling between the two levels,

$$(H_{11} - H_{22})^2 \gg 4H_{12}^2, \quad (151)$$

assuming $H_{11} > H_{22}$, we have

$$E_1 = H_{11} + H_{12}^2 / (H_{11} - H_{22}) \quad (152)$$

and

$$E_2 = H_{22} - H_{12}^2 / (H_{11} - H_{22}) \quad (153)$$

for energies, and

$$C_2 / C_1 = H_{12} / (H_{11} - H_{22}), \quad (154)$$

where

$$C_1 \gg C_2, \quad (155)$$

for the wave function Ψ_1 , and

$$C_1/C_2 = H_{12}/(H_{11}-H_{22}), \quad (156)$$

where

$$C_2 \gg C_1, \quad (157)$$

for the wave function Ψ_2 .

We see that after we turn on the interaction between these two levels, level 1 is raised, and the corresponding wave function is no longer pure ϕ_1 but has a small amount of ϕ_2 mixed into it. Also, the level 2 is lowered, and the corresponding wave function is no longer pure ϕ_2 but has a small amount of ϕ_1 mixed into it (Fig.5).

In the strong bonding case,

$$(H_{11}-H_{22})^2 \ll 4H_{12}^2. \quad (158)$$

In particular, in the degenerate case

$$H_{11} = H_{22} \quad (159)$$

where the bonding is strongest, we have

$$E = H_{11} \pm H_{12} \quad (160)$$

for energies, and

$$C_1 = \pm C_2 \quad (161)$$

for wave functions. That is, in the strong bonding (degenerate) case, the two levels are perfectly mixed with 50% occupation on each of the basis functions (Fig.6).

With this simple model calculation in mind, we are ready to discuss the much more sophisticated slab calculation. It turns out that the basic physical bonding mechanisms are essentially the same in these two cases. In other words, the two-level picture can be easily generalized into a many-level picture.

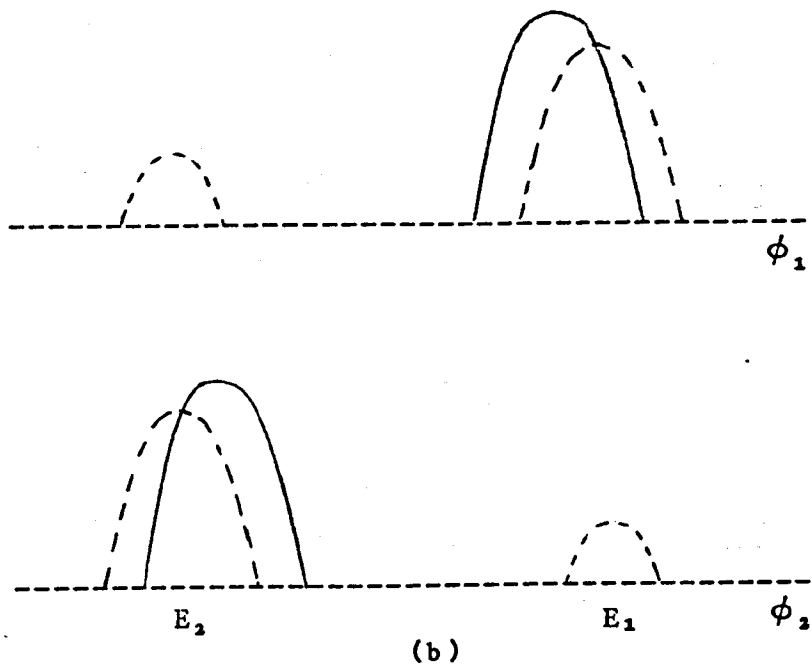
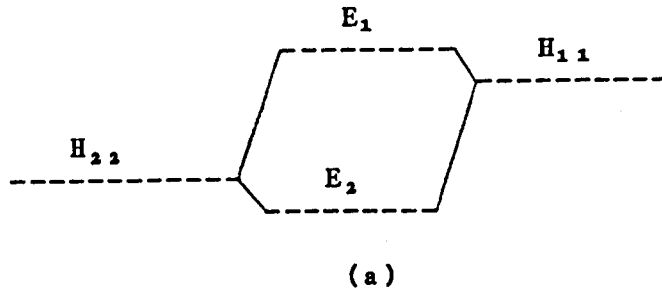
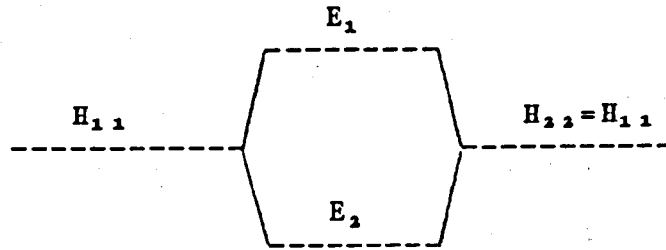
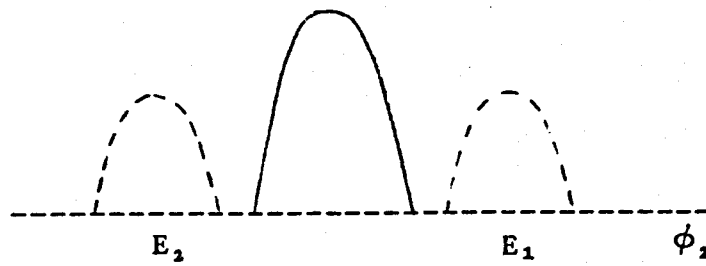
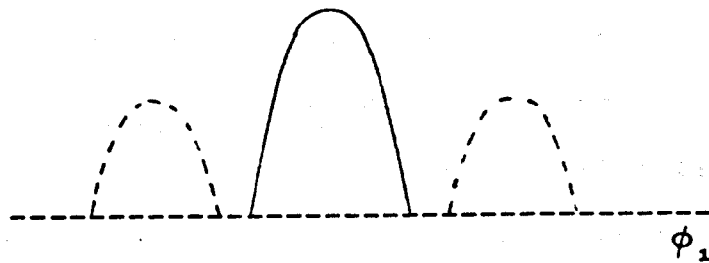


Fig.5 Two-level bonding. Weak coupling.
 (a) Energy splitting.
 (b) Occupation probability on ϕ_1 and ϕ_2 .



(a)



(b)

Fig.6 Two-level bonding. Strong coupling (degenerate case).
 (a) Energy splitting.
 (b) Occupation probability on ϕ_1 and ϕ_2 .

Density of States

The nature of the surface chemical bond is easily clarified by examining layer-projected DOS's (142) given in Fig.7 and orbital-layer-projected DOS's (141) given in Fig.8-Fig.10. In Fig.7, we also show the corresponding DOS's for a clean Fe slab for comparison (an independent calculation for a clean, unrelaxed, five layer Fe slab was also performed).

The DOS of the oxygen layer has pronounced features in a 4-eV-wide distribution centered 5.5 eV below E_F , in good agreement with the experimental UPS results [7,8]. In addition to these bonding levels below the 3d bands in Fig.7, the adlayer DOS has a broad band of antibonding levels that extend about 2 eV above E_F . The unoccupied portion of these bands serve as final states for electrons excited from the bonding 2p band by EELS [10]: a prominent transition is observed near 6 eV. Appearance potential spectroscopy (APS) measurements [65] have also identified an empty band of oxygen-like states about 1 eV above E_F .

Oxygen adsorption substantially reduces the Fe surface DOS in the Fe d band region, and also produces the Fe surface DOS in the O p band region. The magnitudes of these effects are directly correlated to the strength of Fe-O hybridization. These features of the surface DOS are expected from the two-level bonding model. The reduction

of the d band emission, which is correlated to the reduction of the corresponding DOS, was observed in UPS experiments [7,8]. Though the DOS's of deeper layers have a bulk-like appearance, however, hybridization is not negligible for subsurface Fe atoms, since oxygen adatoms are in close proximity to them. Note that the Fe-O bond length [9] is actually smaller for the second plane, 2.02 Å, than for the first plane, where it is 2.08 Å. The O 2p peaks are very weak in the film center, as expected. The DOS of the central layer of O/Fe agrees well with the corresponding DOS of the clean Fe film (Fig.7), and agrees well with the calculated bulk Fe DOS [27,28], too.

The planar DOS's in Fig.7 can be resolved into atomic-orbital components for further insight concerning the surface bond. We present Fe 3d and O 2p DOS's in Fig.8-Fig.10. We begin with the top-layer-Fe DOS's in Fig.8. Among the 3d orbitals, both $3z^2-r^2$ and x^2-y^2 have strong, narrow DOS peaks about 1.9 eV below E_F for majority spin: compare Fig.8. Only very weak O 2p hybridization occurs for the $3z^2-r^2$ orbital, presumably because of its vertical orientation, which minimizes its interaction with oxygen atoms positioned in hollow sites. The xz, yz orbitals (equivalent by symmetry) have somewhat stronger interaction with oxygen, but certainly do not dominate the bonding as suggested earlier [10]. Instead it is the

planar orbitals, of x^2-y^2 and xy character, that have the strongest hybridization with oxygen, and hence the largest DOS peaks below the d bands. This result is consistent with the nearly co-planar geometry assumed in the calculation. In particular, the xy orbital, with lobes directed into the four-fold hollow sites, has the strongest hybridization with O 2p levels. Note the intense DOS structure below -4 eV, as well as the strong repulsion of $3d_{xy}$ levels towards higher energies. Both of these features are characteristic of strong two-level bonding. Also, because the shape of the xy DOS in the O 2p region is so similar to that of the $2p_x$, $2p_y$ band of the adlayer, and because the amplitude of the xy DOS in the O 2p region is as high as that of the O $2p_x$ ($2p_y$), which is the feature of strong two-level bonding, we conclude that the primary bonding mechanism is Fe d_{xy} /O p_x, p_y . In the EELS study of Sakisaka *et al* [10], it was observed that two Fe energy-loss peaks, 5 and 8 eV respectively, were strongly affected by oxygen at the chemisorption stage. The atomic orbitals involved were first assigned to be $3d_{xz}$ (xy, xz, yz), and further referred to as xz and yz . Our calculation shows, however, that it is not the xz , yz but the xy orbital of Fe which is most strongly affected by the oxygen, and thus is mainly responsible for chemical bonding at the chemisorption stage. In fact, if we chose

oxygen 2p planar orbitals as $p_x \pm p_y$ instead of p_x, p_y (rotating the lobes 45 degrees), as we did in Fig.11 and Fig.12 (diagonalization will automatically make this kind of linear combination if needed), the bonding mechanism will become more obvious. This planar bonding, however, is k -dependent. The atomic wave function at the lattice site m , $a_i(r-m)$, is modulated by an exponential factor $\exp(-ik \cdot m)$ in the Bloch function summation. Thus the sign of this atomic wave function may change, and this sign change may affect the superposition of this wave function and the neighboring wave function, thus changing the bonding situation. The DOS given in Fig.8 is k -integrated, that is, after summing over all possible k points: some of the k points correspond to strong bonding, while others correspond to weak bonding. This k -dependent bonding is shown in Fig.11 and Fig.12. Also, geometrical considerations suggests that the p_z orbital should play a minor role.

Now consider the orbital DOS's of the second Fe layer. In this case, as seen in Fig.9, only $3z^2-r^2$ DOS has a sizeable amplitude below -4 eV. Moreover, the DOS shape there resembles the O $2p_z$ and not the O $2p_x-2p_y$ band on the adlayer. We may infer that oxygen bonds to subsurface Fe atoms according to the scheme Fe $d_{3z^2-r^2}/O 2p_z$. This mechanism is understandable considering the vertical

relationship of the two atoms (Fig.13). In contrast to the planar bonding of surface Fe/O, this vertical bonding is virtually k -independent, reminding us that k is a two dimensional vector in the XY plane. In spite of this k -independent bonding nature, the shorter bond length and the more extended d_z^2 function, this Fe(S-1) $d_{3z^2-r^2}/O$ $2p_z$ bonding is not as strong as the Fe(S) d_{xy}/O p_{x+y} bonding because the former has fewer nearest neighbors (1:4) and fewer p bands involved (1:2).

Finally, Fig.10 shows that oxygen hybridizes very little with Fe orbitals at the slab center. Although a slightly thicker slab would be required to completely eliminate hybridization at the center, as discussed later in the sections of occupancies and magnetism, our slab is thick enough to provide nearly bulk-like electronic structure at the central plane. In Fig.10 it is shown that the DOS of xz and yz are the same, as required by symmetry considerations. In addition to that, the DOS of the xy orbital is almost the same as the DOS of xz and yz . There is no symmetry reason for that in the slab case unless the slab is thick enough that the center plane is bulk-like.

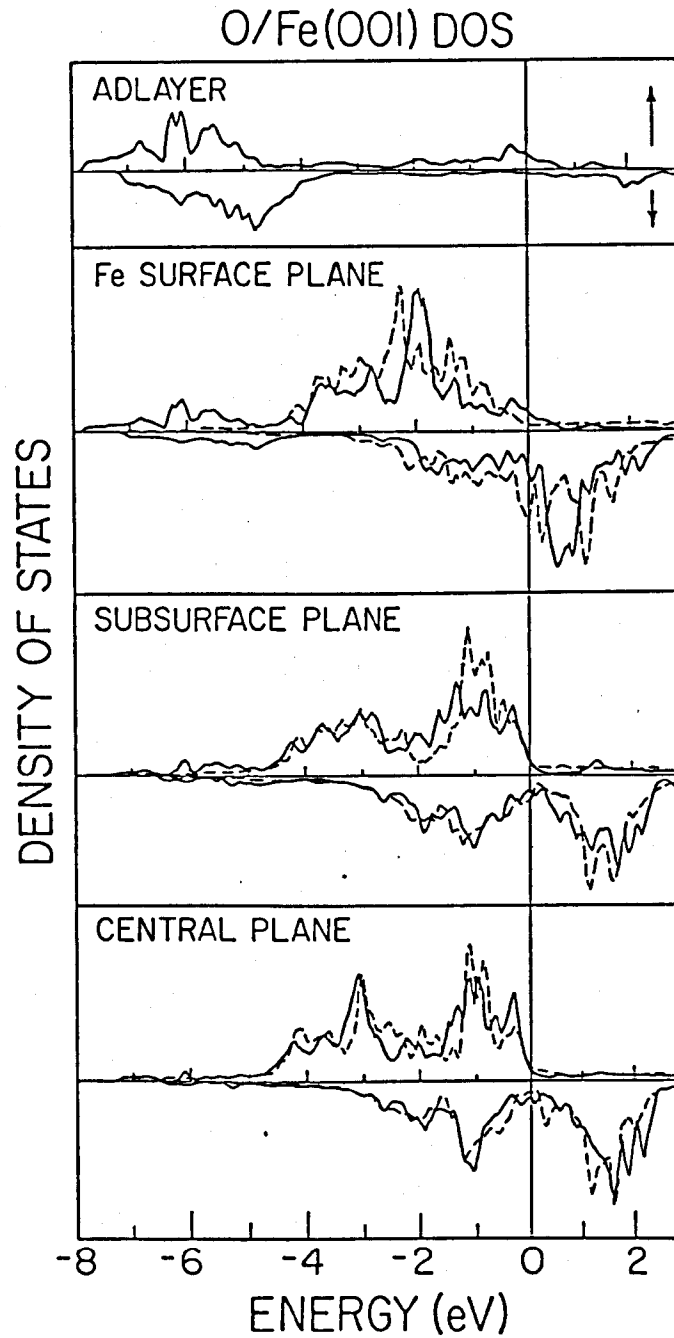


Fig.7 Layer-projected DOS's of O/Fe(001). E_F is the energy zero. The vertical scale is arbitrary. Majority-(Minority-) spin DOS's are indicated by $\uparrow(\downarrow)$. Results obtained for the clean Fe(001) film (shifted to align E_F) are shown with dashed lines.

(a) SURFACE DOS

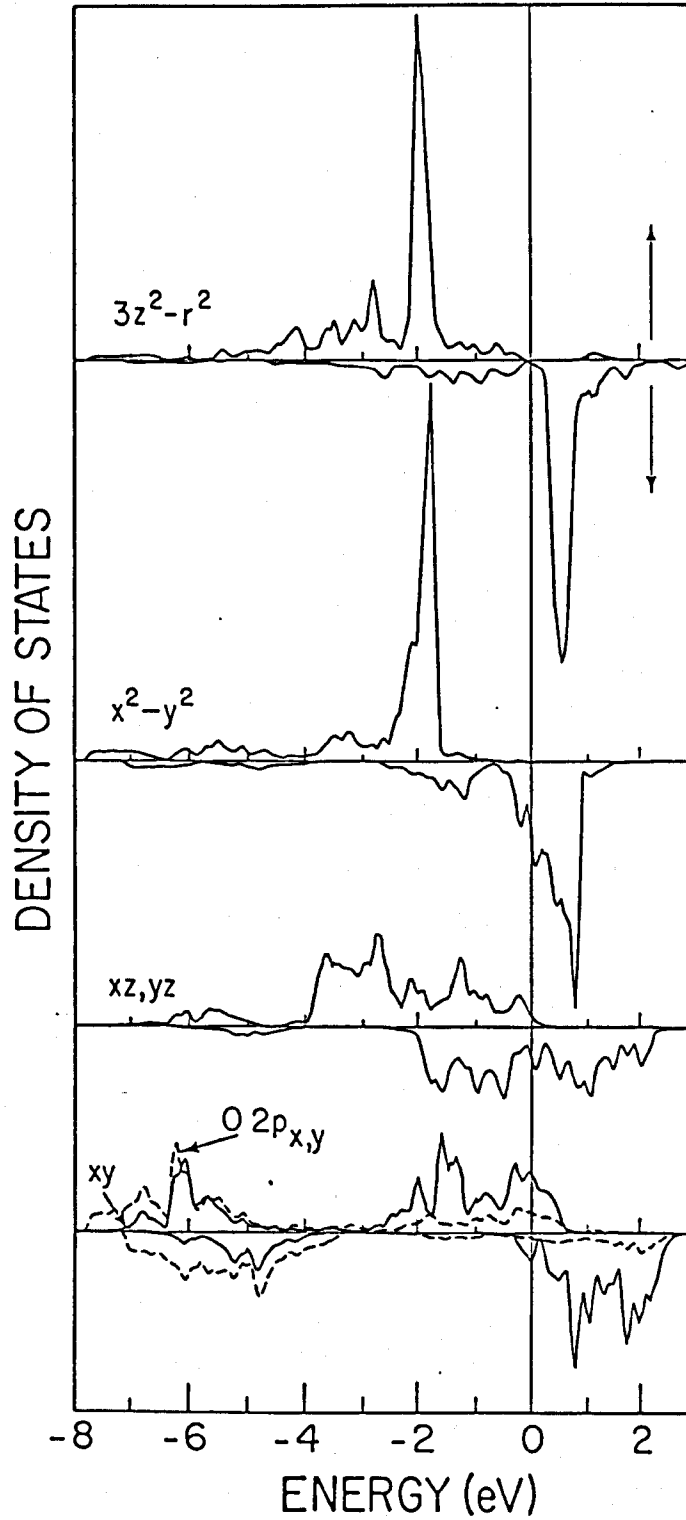


Fig.8 Fe 3d-orbital DOS's of O/Fe(001) for surface plane. For comparison purposes, the O 2p_x(2p_y)-orbital DOS's are also shown (dashed lines).

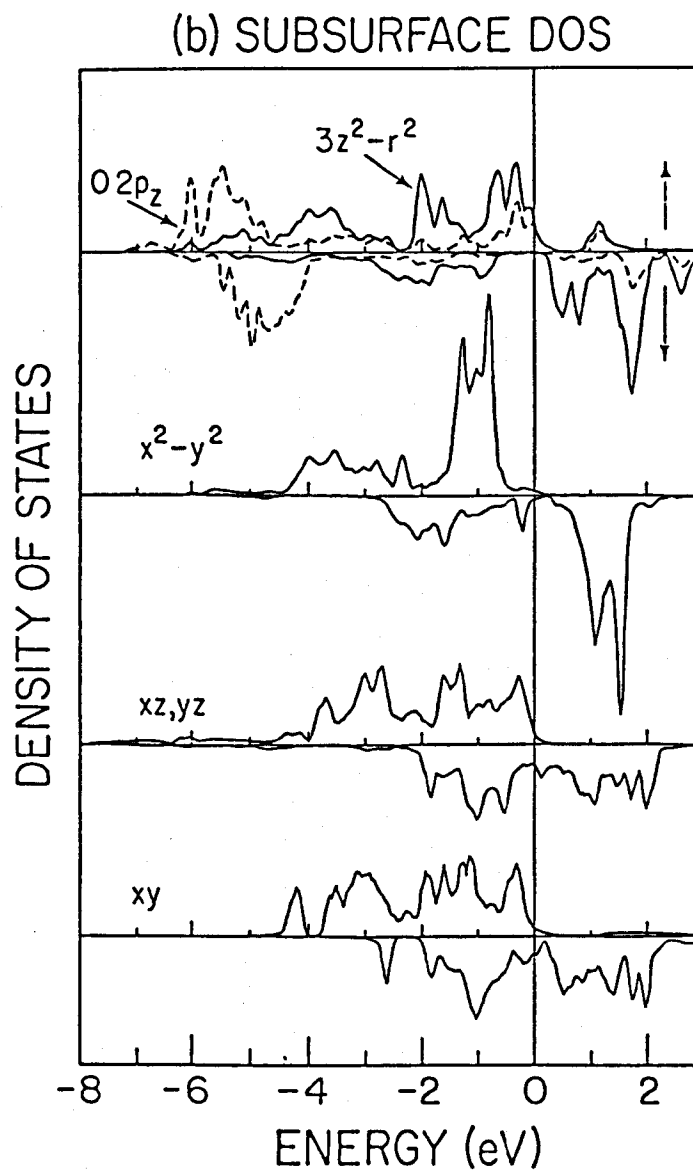


Fig.9 Fe 3d-orbital DOS's of O/Fe(001) for subsurface plane. For comparison purposes, the O $2p_z$ -orbital DOS's are also shown (dashed lines).

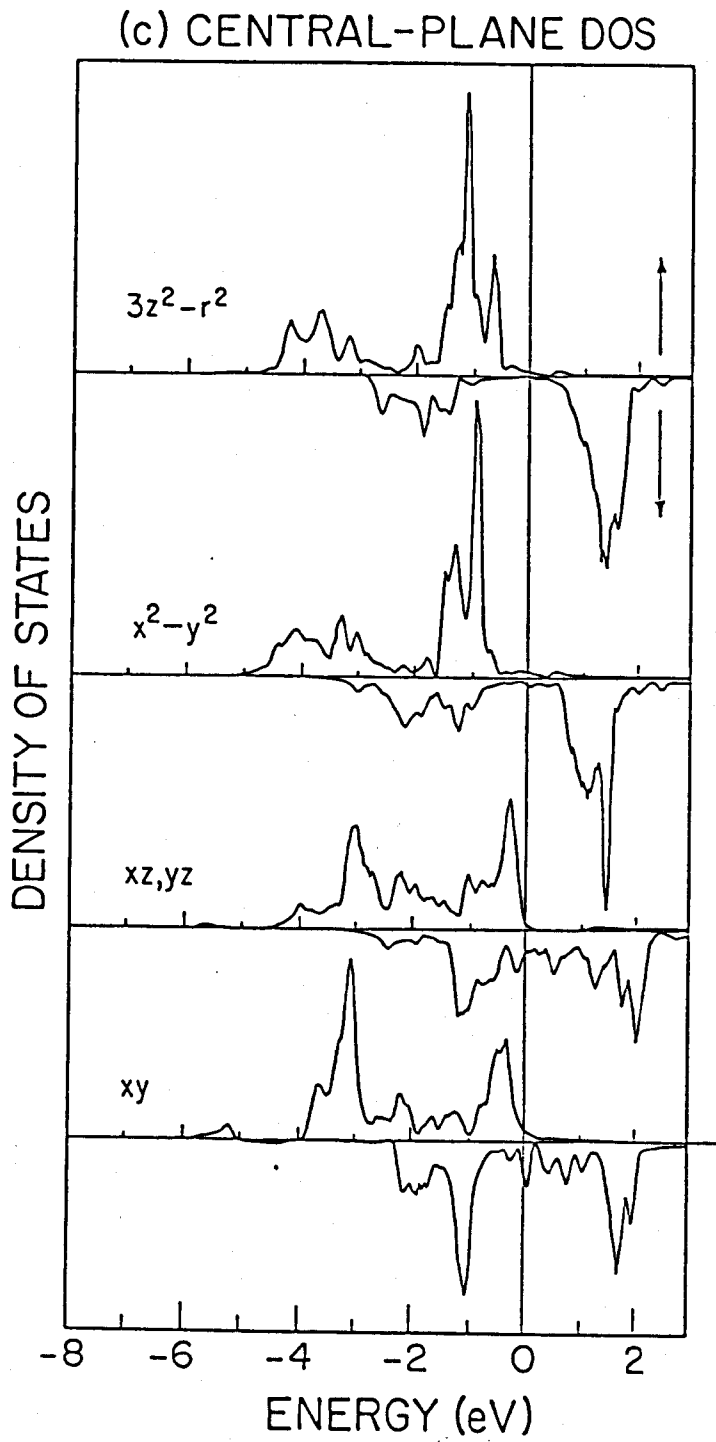


Fig.10 Fe 3d-orbital DOS's of O/Fe(001) for the central-plane.

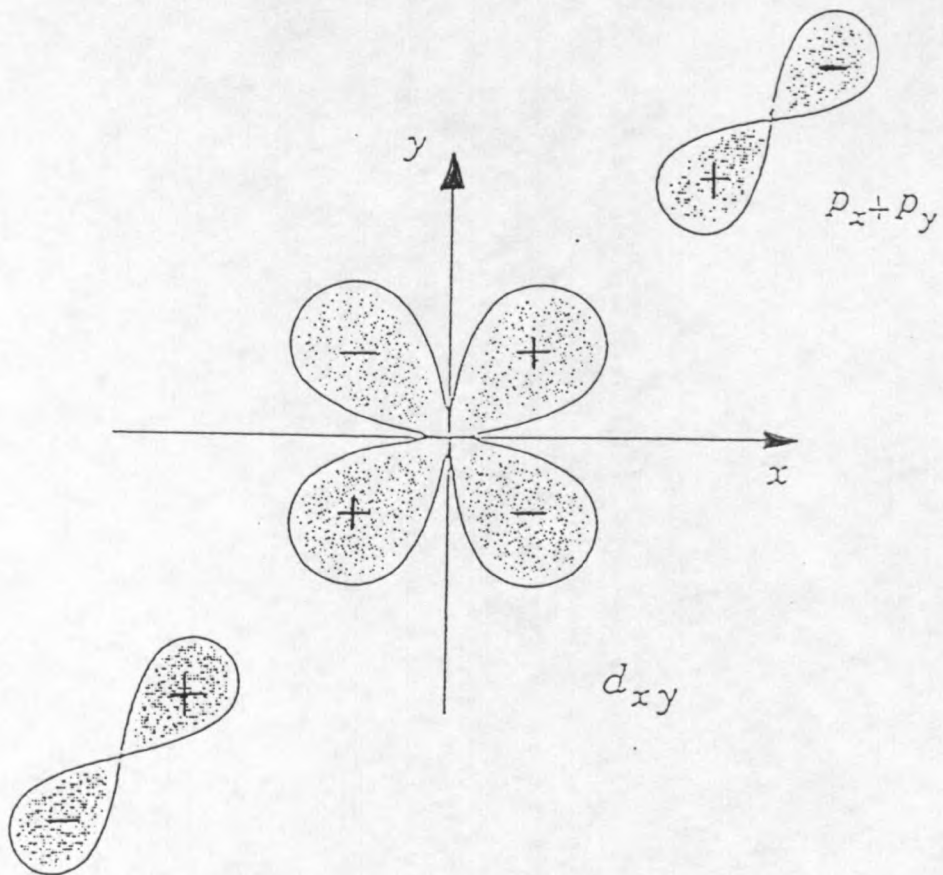


Fig.11 Planar bonding. $\text{Fe(S)} d_{xy}/0 p_x + p_y$. $k = \pi/(2a)(1,1)$.

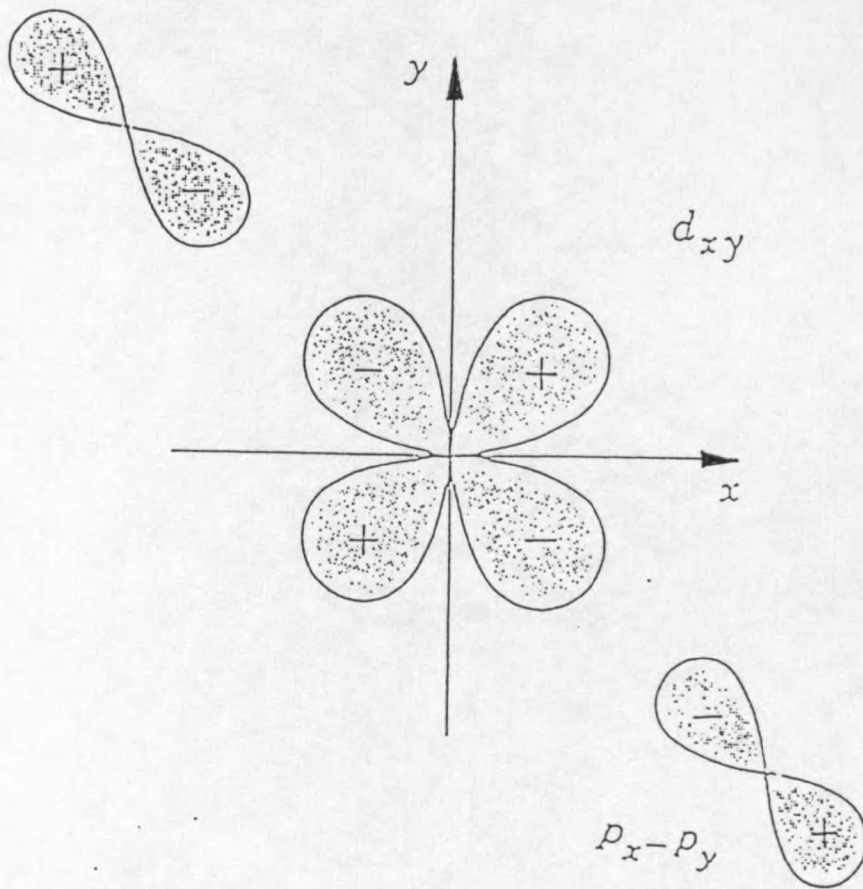


Fig.12 Planar bonding. Fe(S) $d_{xy}/0$ $p_x - p_y$. $k = \pi/(2a)(-1, 1)$.

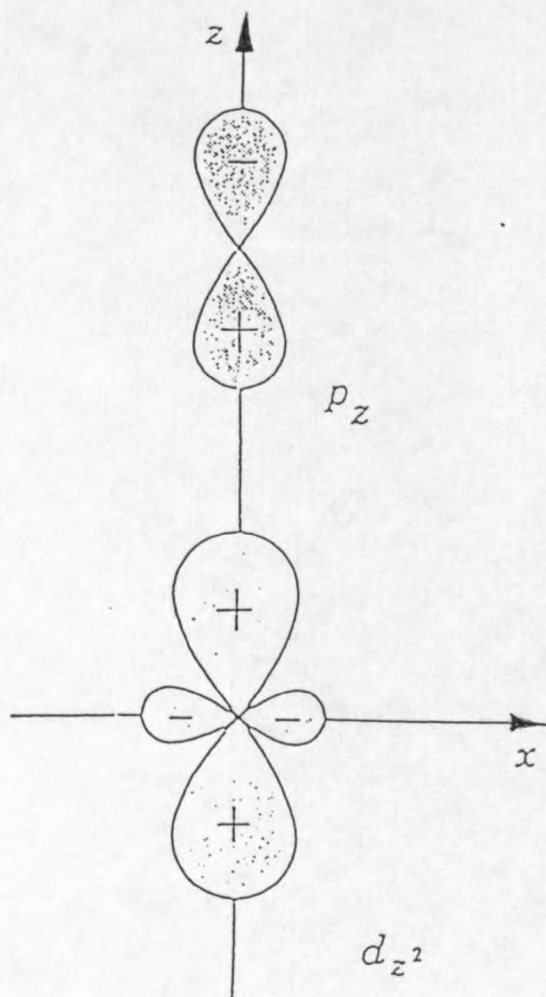


Fig.13 Vertical bonding. Fe(S-1) $d_{z^2}/0 p_z$. k -independent.

Atomic-orbital Occupancies

Occupation numbers (141-144) in the Lowdin basis of orthogonalized atomic orbitals are given in Table 4. The d-orbital occupancies are affected by both the surface potential and the oxygen adlayer. At the surface of the clean film, all d-orbital occupation numbers are slightly larger than their central-plane values except for the xz , yz orbitals. The central-plane results should be representative of the bulk. The surface-induced increase is due to dehybridization [49]: nominal d-band levels have higher d character at the surface. Because the various d-orbitals on a given atom have similar occupancies, the charge density is nearly isotropic in the d shell (Fig.14). On the other hand, the spin density shown in Fig.15 is anisotropic, reflecting the dominance of e_g ($3z^2-r^2, x^2-y^2$) orbitals (Table 5).

Oxygen adsorption perturbs the metal d-orbital occupancies, especially those involved in the Fe-O bonding. Within the (metal) surface plane, the xy occupation number is reduced from 1.40 to 1.09 electrons per atom, while the subsurface $3z^2-r^2$ electron count falls from 1.31 to 1.21 when oxygen is present. Both decreases are due to O 2p/Fe 3d level repulsion, as predicted by the two-level bonding model, and a transfer of d character into antibonding levels above E_F . The non-bonding x^2-y^2

orbital experiences almost no oxygen-induced changes of occupation. Finally, the surface xz (yz) occupancy increases from 1.38 to 1.47 electrons per atom when oxygen is adsorbed. The total number of atomic d electrons n_d is reduced by 0.26, 0.02, and 0.12 on the surface, subsurface, and central planes of the oxygenated film, respectively.

Surface- and oxygen-induced charge transfer can be studied using the results in Table 4. In addition to the changes in n_d noted above, results for n_{sp} and total valence occupation $n=n_d+n_{sp}$ are given. While the clean metal film exhibits charge neutrality (8 valence electrons per atom) to within 0.03 electron per atom, oxygen attracts a significant number of electrons from the surface and subsurface layers. In particular, 0.63 electrons are transferred from the metal to each oxygen atom, leaving behind a charge deficit of 0.52, 0.05, and 0.11 on planes S, S-1, and C, respectively. Thus in addition to the covalent bonding between oxygen and iron, we see that ionic bonding also exists. Although the meaning of these occupation numbers is somewhat ambiguous, due to the fact the Lowdin orbitals are no longer pure atomic Block orbitals, the 0.11 electrons deficit per atom at the central layer is an indication that a thicker slab is needed to maintain charge neutrality of the central

layer of the slab. However, such a large transfer of charge is not unreasonable within our finite-thickness slab model, given the huge electronegativity of oxygen, which is often assigned a formal charge of 2 or 3 electrons in compound formation, or equivalently given the huge work function difference between the clean Fe slab and the oxygen monolayer: 4.4 eV vs. 8.0 eV (an auxiliary calculation for a monolayer of oxygen with Fe lattice constant was also performed). One expects a large work-function shift compared with the clean Fe slab when the Fe and O slabs are brought together, creating a dipole layer at the interface. We found the value $\Delta\Phi = 1.4$ eV. The work function we calculated for Fe, is 4.4 eV, in excellent agreement with the experimental values 4.4 eV [68] and 4.3 eV [69]. Observed values [8,10] of $\Delta\Phi$ for O/Fe(001) in the chemisorption stage are no larger than 0.25 eV, perhaps due to the incorporation of oxygen below the ideal Fe surface at full oxygen coverage (1x1). Our calculation provides a test of the oxidation model we used and thus may help to clarify the oxidation process of the Fe surface.

Table 4. Occupation numbers per atom for a clean five-plane Fe(001) film, Fe_s, and a five-plane film with oxygen atoms positioned in the four-fold hollow sites on both faces, O/Fe_s. The iron surface, subsurface and center planes are labeled S, S-1, and C. The oxygen adsorbate layer is denoted as A.

Film	Layer	$3z^2-r^2$	x^2-y^2	$xz(yz)$	xy	n_d	n_{sp}	n
Fe _s	S	1.31	1.31	1.38	1.41	6.80	1.23	8.03
	S-1	1.28	1.22	1.42	1.40	6.74	1.25	7.99
	C	1.27	1.29	1.41	1.35	6.74	1.23	7.97
O/Fe _s	A						6.63	6.63
	S	1.21	1.31	1.47	1.09	6.54	0.94	7.48
	S-1	1.21	1.27	1.43	1.43	6.72	1.23	7.95
	C	1.21	1.28	1.35	1.42	6.62	1.27	7.89

Table 5. Magnetic moments per atom for a clean five-plane Fe(001) film, Fe_s, and a five-plane film with oxygen atoms positioned in the four-fold hollow sites on both faces, O/Fe_s. The iron surface, subsurface and center planes are labeled S, S-1, and C. The oxygen adsorbate layer is denoted as A.

Film	Layer	$3z^2-r^2$	x^2-y^2	$xz(yz)$	xy	n_d	n_{sp}	n
Fe _s	S	0.63	0.58	0.54	0.49	2.79	0.10	2.89
	S-1	0.58	0.62	0.38	0.42	2.37	-0.06	2.31
	C	0.65	0.59	0.42	0.46	2.53	-0.04	2.49
O/Fe _s	A						0.24	0.24
	S	0.73	0.67	0.44	0.64	2.92	0.010	2.93
	S-1	0.56	0.63	0.46	0.48	2.58	-0.006	2.57
	C	0.69	0.59	0.50	0.42	2.72	-0.004	2.72

Magnetism

Recent spin-resolved photoemission experiments [68] suggest that oxygen removes the surface magnetism of Ni(110), while it has only slight influence on the magnetism of a Fe-based glass ($\text{Fe}_{82}\text{B}_{12}\text{Si}_6$). (Surprisingly enough, even in this Fe glass case, at chemisorption stage, it was observed that there is an oxygen induced photoemission peak 5.5 eV below E_F , and a reduction of Fe 3d peak, in agreement with oxygen on Fe(001) surface [7,8]. This seems to be a universal feature of O chemisorption on Fe, no matter what kind of Fe it is.) Our results for the orbital-layer-resolved magnetic behavior (141-143,145) of O/Fe(001) and clean Fe(001) are given in Table 5. Note the substantial surface enhancement of the magnetic moment of the clean metal film (16% increase compared with the center-plane value). This enhancement is not removed by the adsorbed oxygen. The magnetic moment per surface Fe atom, m , increases slightly from the corresponding value of the clean Fe slab (from 2.89 to 2.93 μ_B). Thus oxygen adsorption does not produce magnetically dead layer. The magnetic moments of subsurface and central layer are also increased from 2.31 to 2.52 and from 2.49 to 2.68 μ_B , respectively. This indicates that the slab is not thick enough to lead central layer bulk-like magnetically. Apparently, the

interaction between oxygen adsorbate and Fe substrate is very strong and has longer range than the perturbation introduced by the surface. The calculated clean Fe slab magnetic moments, m 's, agree well with the m 's calculated by Ohnishi et al [69,70]. They found for a five layer clean Fe slab, the magnetic moments are 2.94, 2.32, and 2.52 μ_B , for surface (S), subsurface (S-1), and center (C) layer, respectively [69]. They also found for a seven layer clean Fe slab, that the magnetic moments are 2.98, 2.35, 2.39, and 2.25 μ_B , for S, S-1, S-2, and C layer, respectively [70]. The oxygen adlayer itself, in our calculation, is spin-polarized, with a magnetic moment of 0.24 μ_B per atom, about 8% of the value on a surface Fe atom. This is not surprising, however, if we remind ourselves that the ground state is 3P_2 for an oxygen atom and is $^3\Sigma_g^-$ for an oxygen molecule. Both of these have magnetic moments.

Charge and Spin Densities

The self-consistent charge density, $\rho_{\uparrow}(r)+\rho_{\downarrow}(r)$, and spin density, $\rho_{\uparrow}(r)-\rho_{\downarrow}(r)$, are shown in Fig.14 and Fig.15. Charge-density contours differing by the ratio 1.414 are drawn in a (110) plane normal to the surface. Spin-density contours differing by a factor of 2 are also given. Note that these figures have a bulk-like appearance below the

Fe-O interface. At the interface, covalent bonds between oxygen and Fe atoms in the first and second metal layers are evident in the buildup of charge along the internuclear axes. Because the oxygen layer is located deep within the metal surface, a definite smoothing of the charge-density corrugation is obtained in the vacuum region. The spin density, Fig.15, is also smoothed by the oxygen, which itself acquires a small magnetization. The adsorption does not quench the surface magnetism of the substrate, though the eruptions into vacuum noted on the clean surface [70] are absent. Some weak, negative magnetization is found between neighboring Fe atoms.

Surface-state Bands

To determine surface bands on O/Fe(001), we selected states in the IBZ which had more than 60% occupation probability (146) on the Fe-O bilayer. These states were divided further into weak and strong surface states, the latter having Fe-O occupation greater than 80%. These bands are shown in Fig.16 and Fig.17. As expected, strong surface bands are found in the range 4 to 8 eV below E_F , that is, just below the Fe 3d bands. These oxygen-like bands may be described as bonding levels, and disperse as simple tight-binding energy bands on p orbitals. There are two sets of p bands for each spin direction corresponding

to symmetric (Fig.16) and antisymmetric (Fig.17) combination of bonding levels on the two equivalent faces of the slab. The energy splitting between symmetric and antisymmetric surface state bands is a measure of the interaction between the two surfaces of the slab. If this splitting vanishes, the slab is said to be thick enough in this respect. This is essentially true in our calculation, as is shown by Fig.16 and 17. In these figures, the p_z band extends as follows: X_2, M_2, Γ_2 : it hybridizes with the p_x (p_y) band along Γ (Y). The p_x, p_y bands are degenerate at M_2 and Γ_2 , with p_x being lower along Y and Γ . The p_z band hybridizes with the even band p_{x+y} along Σ . Exchange splittings in the O 2p bands vary from 0.5 to 1.0 eV.

The oxygen-induced bands 4 to 8 eV below E_F should be resolvable using ARPES [16]. Their energetic separation from the bulk Fe levels and their relatively flat dispersion make them good candidates for observation. The use of polarized light together with the selection rules [17] for ARPES would facilitate the identification of bands along the Δ and Σ lines, which contain mirror planes. In particular, even bands labeled Δ_1 and Σ_1 are excited by light polarized in the respective mirror planes, while the odd bands, Δ_2 and Σ_2 , require a component of the vector potential perpendicular to these

planes. A broad oxygen-induced resonance was observed 5.5 eV below E_F in angle-integrated photoemission data [8].

A second set of surface bands is also seen in Fig.16 and Fig.17. These are located in the Fe 3d bulk continuum, and have higher Fe character than the bands just discussed. Because of their large Fe amplitudes, the bands have large exchange splittings. The actual values depend on the degree of surface localization as well as the Fe character. In comparison with clean Fe(001) [70], the oxygenated surface has fewer surface-state bands in the 3d region. The greatest concentration is found 1.7 to 2 eV below E_F . (We discuss only majority-spin bands). A $X_1Y_1M_1 \sum_1$ band is particularly prominent. It is quite flat, is centered near -1.9 eV, and has mainly $3z^2-r^2$ character. One expects this band to be only weakly affected by oxygen atoms located in four-fold hollow sites. An x^2-y^2 surface band $Y_1M_1 \sum_2$ is also strong. It is centered near -1.8 eV. See Fig.8 of surface orbital-projected DOS of these two orbitals. Weak bands are found near M_4 (xy character), Γ_4 (xy) near the d-band edge, and along Δ_1 near X_1 ($3z^2-r^2$, x^2-y^2). Some of the weak surface states may convert to bulk states in thicker slabs. The agreement or disagreement between calculated surface bands (especially oxygen-like bands) and ARPES should greatly help to identify the chemisorption/oxidation model.

CHARGE DENSITY

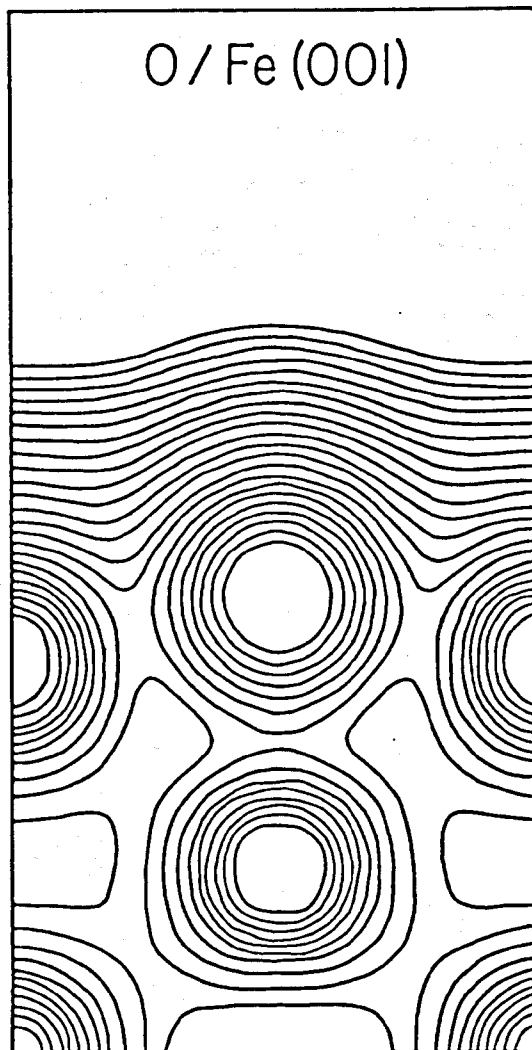


Fig.14 Charge-density contours in the (110) plane normal to the surface of the O/Fe₂(001) slab. Contour values increase by the factor 1.414 as the core region is approached.

SPIN DENSITY

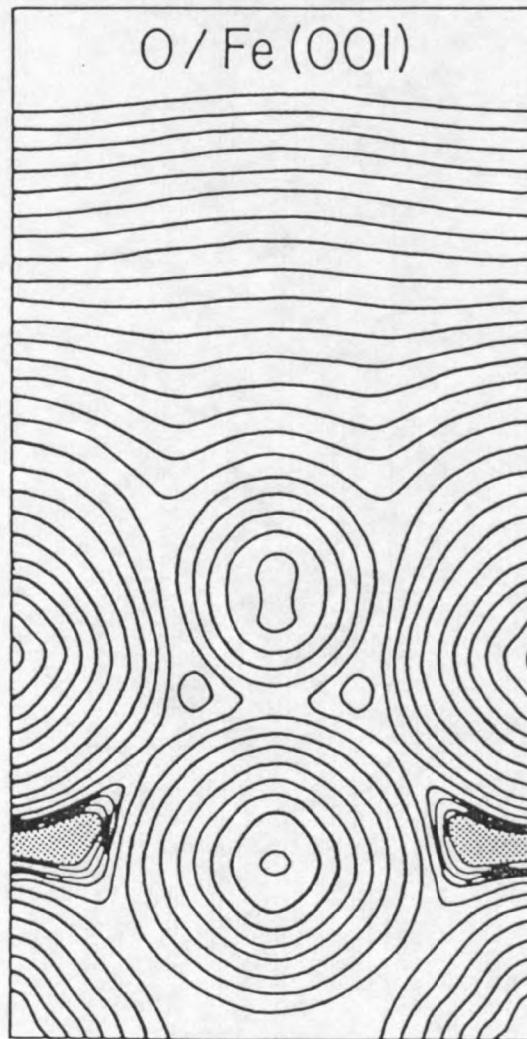


Fig.15 Spin-density contours for O/Fe(001), plotted in the (110) plane. Successive contours have the ratio 2, increasing towards the nuclei. Weak negative magnetization is indicated by the shading.

(a) SYMMETRIC SURFACE BANDS

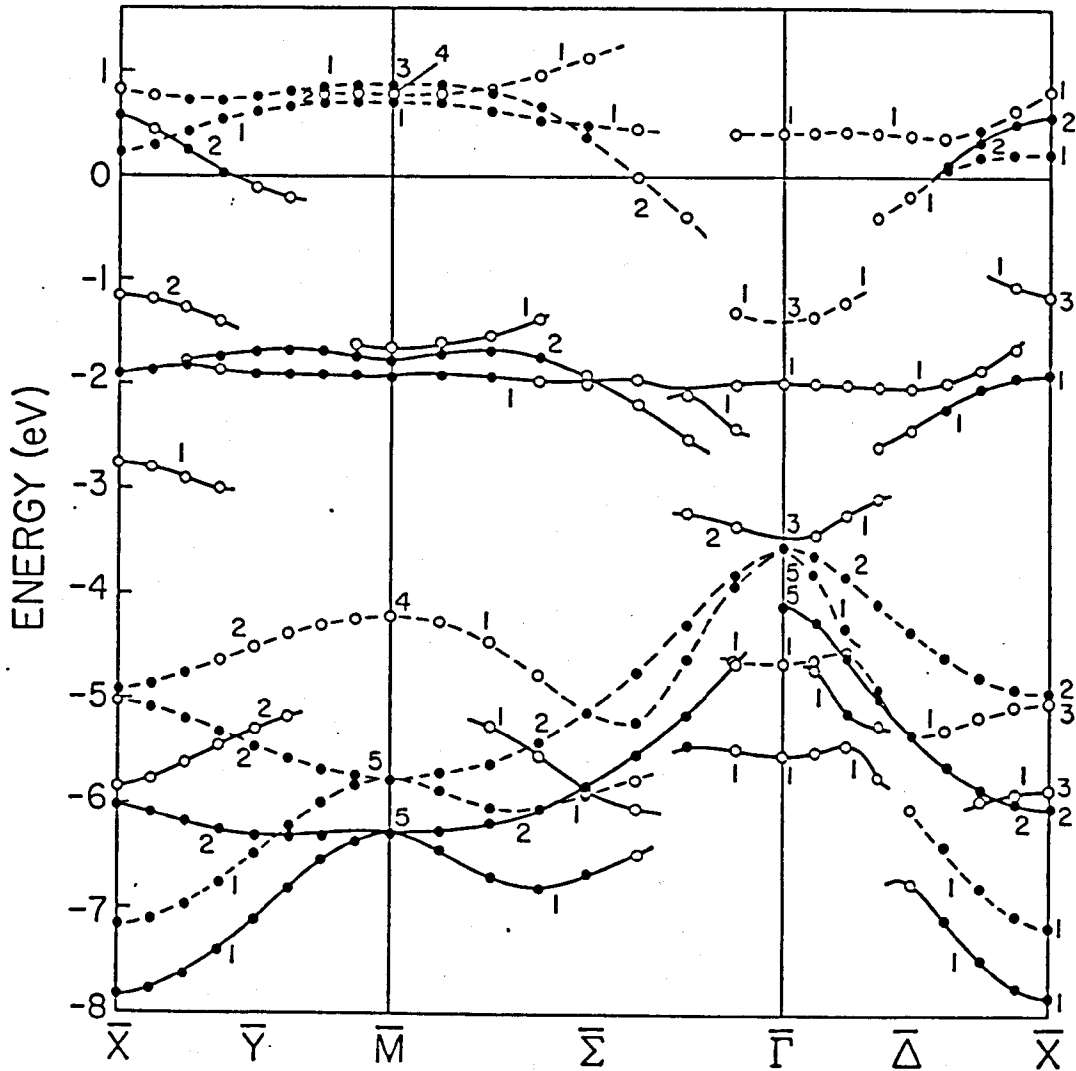


Fig.16 Spin-split symmetric surface bands of O/Fe(001). Strong surface states (filled circles) have more than 80% Fe-O interface character, weak states (open circles) more than 60% but less than 80%. $\uparrow(\downarrow)$ bands are indicated with full(dashed) lines. E_F is the energy zero. Along the symmetry lines \bar{Y} , $\bar{\Sigma}$ and $\bar{\Delta}$, bands labeled 1 are even with respect to the appropriate vertical mirror plane. Those labeled 2 are odd.

(b) ANTISYMMETRIC SURFACE BANDS

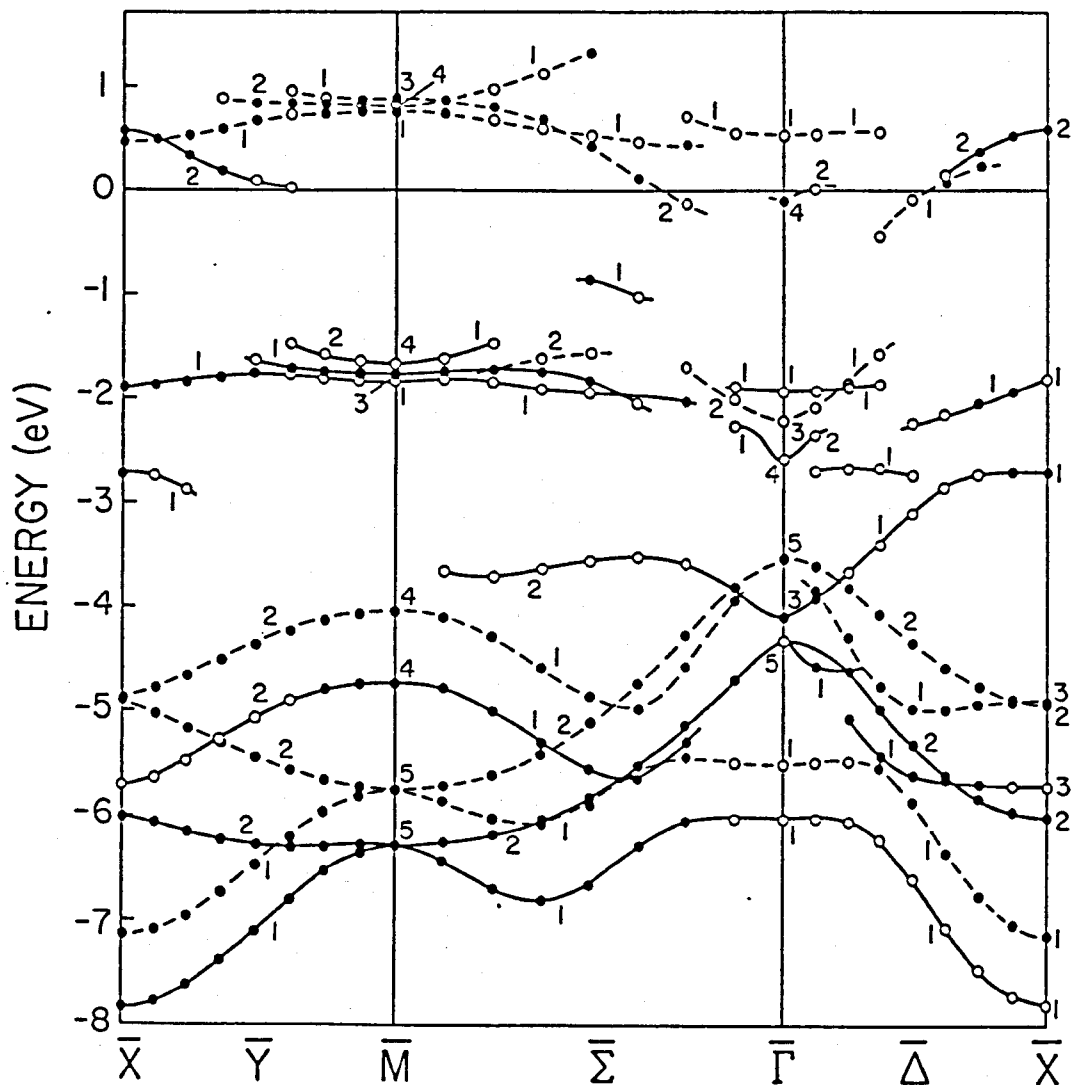


Fig.17 Spin-split antisymmetric surface bands of O/Fe(001). Strong surface states (filled circles) have more than 80% Fe-O interface character, weak states (open circles) more than 60% but less than 80%. $\uparrow(\downarrow)$ bands are indicated with full(dashed) lines. E_F is the energy zero. Along the symmetry lines \bar{Y} , $\bar{\Sigma}$ and $\bar{\Delta}$, bands labeled 1 are even with respect to the appropriate vertical mirror plane. Those labeled 2 are odd.

CHAPTER 4

SUMMARY AND FUTURE STUDY

Summary

The electronic structure and magnetism of a $p(1 \times 1)$ chemisorbed oxygen layer on the Fe(001) surface was studied by the SCLM method. The interface geometry was suggested by Legg et al based on a previous LEED analysis [9].

We found oxygen-induced peaks centered 5.5 eV below E_F and 1 eV above E_F , and a reduction of the Fe surface DOS in the 3d-band region, in good agreement with UPS [7,8,68] and EELS [8] and APS [65] experiments.

We found that the oxygen atoms have significant bonding to both the surface and subsurface Fe layers. Planar bonding is primarily due to the surface Fe $3d_{xy}$ orbital and the adlayer O $2p_{x+y}$ orbitals. Vertical bonding of O to subsurface Fe is accomplished through Fe $3d_z$ and O $2p_z$ orbitals.

The oxygen adlayer has a magnetic moment of $0.24\mu_B$ per atom, while surface Fe atoms have a moment of $2.93\mu_B$, essentially unchanged from the clean-surface value $2.89\mu_B$. We did not find a magnetically dead layer on the Fe

surface, consistent with spin-resolved photoemission experiment on Fe-based glass [68].

Oxygen atoms have a net charge of 0.6 electron drawn from the surface and subsurface iron planes. As a result the work function increases 1.4 eV compared with the clean substrate, in disagreement with measurements on O/Fe(001) [8,10], which obtain much smaller shifts. The discrepancy may be due to absorption of oxygen into the metal.

Oxygen-like energy bands were obtained 4 to 8 eV below E_F with exchange splittings of 0.5 to 1.0 eV. Another set of surface bands, mainly with the surface Fe character, was found 2 eV below E_F (majority spin). These surface bands should be detectable using ARPES, and this should help to clarify the chemisorption/oxidation model.

Suggestions for Future Study

In order to fully understand the oxidation process of Fe, we have the following suggestions for future study.

1) To calculate energy bands for c(2x2) O/Fe(001), and to compare with ARPES data. It is still an experimental controversy whether the chemisorbed oxygen layer at its maximum coverage forms c(2x2) or p(1x1) structure on the Fe(001) surface.

2) To calculate energy bands for c(2x2) and p(1x1) oxygen layer(s) beneath the Fe(001) surface, and to

compare with ARPES to understand the oxygen incorporation process, about which little is known. In this case, the oxygen-like bands would be quite different from the bands of oxygen on the Fe surface.

3) To calculate the total energy [27,71] of the all possible chemisorption/oxidation configurations, and to understand how the system evolves from the oxygen chemisorption stage to bulk iron oxide. There is a long way to go in this respect. The LDA calculation predicts f.c.c rather than b.c.c. crystalline structure for bulk Fe [72], and this is probably due to the failure of the local density approximation [73].

REFERENCES CITED

- [1] A.J.Pignocco and G.E.Pellissier, *J. Electrochem. Soc.* 112, 1188 (1965).
- [2] P.B.Swell, D.F.Mitchell, and M.Cohen, *Surf. Sci.* 33, 535 (1972).
- [3] Leygraf and S.Ekelund, *Surf. Sci.* 40, 609 (1973).
- [4] T.Horiguchi and S.Nakanishi, *Jpn. J. Appl. Phys. Suppl.* 2, 89 (1974).
- [5] G.W.Simmons and D.J.Dwyer, *Surf. Sci.* 48, 373 (1975).
- [6] K.O.Legg, F.Jona, D.W.Jepson, and P.M.Marcus, *J. Phys. C* 8, L492 (1975).
- [7] K.Y.Yu, W.E.Spicer, I.Lindan, P.Pianetta, and S.F.Liu, *Surf. Sci.* 57, 157 (1976).
- [8] C.F.Brucker and T.N.Rhodin, *Surf. Sci.* 57, 523 (1976).
- [9] K.O.Legg, F.Jona, D.W.Jepson, and P.M.Marcus, *Phys. Rev. B* 16, 5271 (1977).
- [10] Y.Sakisaka, T.Miyano, and M.Onchi, *Phys. Rev. B* 30, 6849 (1984).
- [11] M.W.Roberts and C.S.McKee, *Chemistry of the Metal-Gas Interface* (Clarendon Press, Oxford, 1978).
- [12] F.P.Fehlner and N.F.Mott. *Oxid. Met.* 2, 59 (1970).
- [13] A.B.Anderson, *Phys. Rev. B* 16, 900 (1977).
- [14] M.W.Ribarsky, *Solid State Commun.* 38, 935 (1981).
- [15] H.Adachi, M.Tsukada, I.yasumori, and M.Onchi, *Surf. Sci.* 119, 10 (1982).
- [16] A.M.Turner and J.L.Erskine, *Phys. Rev. B* 30, 2377 (1980).
- [17] J.Hermanson, *Solid State Commun.* 22, 9 (1977).
- [18] J.G.Gay, J.R.Smith, and F.J.Arlinghaus, *Phys. Rev. Lett.* 38, 561 (1977).
- [19] J.R.Smith, F.J.Arlinghaus, and J.G.Gay, *Solid State Commun.* 24, 279 (1977).

- [20] J.R.Smith, J.G.Gay, and F.J.Arlinghaus, Phys. Rev. B 21, 2201 (1980).
- [21] H.Huang and J.Hermanson, to be published in Phys. Rev. B.
- [22] H.Huang, X.Y.Zhu, and J.Hermanson, Phys. Rev. B 29, 2207 (1984).
- [23] X.Y.Zhu, H.Huang, and J.Hermanson, Phys. Rev. B 29, 3009 (1984).
- [24] H.Huang and J.Hermanson, Surf. Sci. 154, 614 (1985).
- [25] H.Huang, J.Hermanson, J.G.Gay, R.Richter, and J.R.Smith, submitted to Phys. Rev. B.
- [26] H.Huang, Z.Duanmu, and J.Hermanson, manuscript in preparation.
- [27] V.L.Moruzzi, J.F.Janak, A.R.Williams, Calculated Electronic Properties of Metals (Pergamon Press, New York, 1978).
- [28] J.Callaway and C.S.Wang, Phys. Rev. B 16, 2095 (1977).
- [29] D.R.Hartree, Proc. Camb. Phil. Soc. 24, 89, 111, 426 (1928).
- [30] V.Fock, Z.Phys. 61, 126 (1930).
- [31] V.Fock, Z.Phys. 2, 795 (1930).
- [32] P.Hohenberg and W.Kohn, Phys. Rev. B 136, 864 (1964).
- [33] W.Kohn and L.J.Sham, Phys. Rev. A 140, 1133 (1965).
- [34] L.Hedin and B.I.Lundqvist, J. Phys. C 4, 2064 (1971).
- [35] S.Lundqvist and N.H.March, Theory of the inhomogeneous electron gas (Plenum Press, New York, 1983).
- [36] J.Callaway, Quantum Theory of the Solid State (Academic Press, New York, 1976).
- [37] J.C.Slater, Phys. Rev. 81, 385 (1951).

- [38] L.H.Thomas, Proc. Camb. Phil. Soc. 23, 542 (1927).
- [39] E.Fermi, Z.Phys. 48, 73 (1928).
- [40] S.H.Vosko, L.Wilk, and M.Nusair, Can. J. Phys. 58, 1200 (1980).
- [41] D.Bohm and D.Pines, Phys. Rev. 92, 609 (1953).
- [42] M.Gell-Mann and K.A.Brueckner, Phys. Rev. 106, 364 (1957).
- [43] J.Hubbard, Proc. R. Soc. A 243, 336 (1957).
- [44] D.Pines and P.Nozieres, The Theory of Quantum Liquids (Benjamin, New York, 1966).
- [45] U. von Barth and L.Hedin, J. Phys. C 5, 1629 (1972).
- [46] D.M.Ceperley, Phys. Rev. B 18, 3126 (1978).
- [47] D.M.Ceperley and B.J.Alder, Phys. Rev. Lett. 45, 566 (1980).
- [48] X.Y.Zhu and J.Hermanson, Phys. Rev. B 27, 2092 (1980).
- [49] X.Y.Zhu, J.Hermanson, F.J.Arlinghaus, J.G.Gay, R.Richter and J.R.Smith, Phys. Rev. B 29, 4426 (1982).
- [50] X.Y.Zhu, Ph.D. Thesis (Montana State University Library, 1983).
- [51] H.F.Schaefer III, The Electronic Structure of Atoms and Molecules (Addison-Wesley, Reading, Mass., 1972).
- [52] R.C.Bardo and K.Ruedenberg, J. Chem. Phys. 59, 5956 (1973).
- [53] F.Herman and S.Skillman, Atomic Structure Calculations (Prentice-Hall, New Jersey, 1963).
- [54] J.K.L.MacDonald, Phys. Rev. 43, 830 (1933).
- [55] W.Y.Ching and C.C.Lin, Phys. Rev. Lett. 34, 1233 (1975).
- [56] E.Lafon and C.C.Lin, Phys. Rev. B 152, 579 (1966).

- [57] R.Chaney, T.K.Tung, C.C.Lin, and E.E.Lafon, J. Chem. Phys. 52, 361 (1970).
- [58] J.Langlinsais and J.Callaway, Phys.Rev. B 5, 124 (1972).
- [59] S.F.Boys, Proc. R. Soc. London 200R, 542 (1950).
- [60] W.T.Cochran, J.W.Cooley, D.L.Favin, H.D.Helms, R.A.Kaenel, W.W.Lang, G.C.Welch, IEEE Trans. Audio AU-15, 45 (1967).
- [61] S.J.Cunningham, Phys. Rev. B 10, 4988 (1974).
- [62] M.Tinkham, Group Theory and Quantum Mechanics (McGraw-Hill, 1964).
- [63] R.S.Mulliken, J. Chem. Phys. 23, 1833 (1955).
- [64] P.O.Lowdin, J. Chem. Phys. 18, 365 (1950).
- [65] S.Andersson and C.Nyberg, Surf. Sci. 52, 489 (1975).
- [66] V.S.Fomenko, in Handbook of Thermionic Properties, p.20, edited by E.G.V.Samsanow (Plenum Press, New York, 1966).
- [67] A.M.Turner, Yu.J.Chang, and J.L.Erskine, Phys. Rev. Lett. 48, 348 (1982).
- [68] W.Schmitt, H.Hopster, and G.Guntherodt, Phys. Rev. B 31, 4035 (1985).
- [69] S.Ohnishi, M.Weinert, and A.J.Freeman, Phys. Rev. B 30, 36 (1984).
- [70] S.Ohnishi, A.J.Freeman, and M.Weinert, Phys. Rev. B 28, 6741 (1983).
- [71] M.Weinert, E.Wimmer, and A.J.Freeman, Phys. Rev. B 26, 4571 (1982).
- [72] H.Krakauer, private communication.
- [73] H.J.F.Jansen, K.B.Hathaway, and A.J.Freeman, Phys. Rev. B 30, 6177 (1984).

MONTANA STATE UNIVERSITY LIBRARIES
arch D378.H86
Self-consistent localized-orbital study

RL



3 1762 00190135 2